catalysts

MDPI

Review

Advances in Magnetically Separable Photocatalysts: Smart, Recyclable Materials for Water Pollution Mitigation

Gcina Mamba * and Ajay Mishra

Nanotechnology and Water Sustainability Research Unit, College of Science, Engineering and Technology, University of South Africa, Florida 1709, Johannesburg, South Africa; mishrak@unisa.ac.za

* Correspondence: gcmamba@gmail.com; Tel.: +27-11-670-9702

Academic Editors: Dionysios (Dion) Demetriou Dionysiou, Giusy Lofrano, Polycarpos Falaras, Suresh C. Pillai, Adrián M.T. Silva and Xie Quan

Received: 16 April 2016; Accepted: 18 May 2016; Published: 20 June 2016

Abstract: Organic and inorganic compounds utilised at different stages of various industrial processes are lost into effluent water and eventually find their way into fresh water sources where they cause devastating effects on the ecosystem due to their stability, toxicity, and non-biodegradable nature. Semiconductor photocatalysis has been highlighted as a promising technology for the treatment of water laden with organic, inorganic, and microbial pollutants. However, these semiconductor photocatalysts are applied in powdered form, which makes separation and recycling after treatment extremely difficult. This not only leads to loss of the photocatalyst but also to secondary pollution by the photocatalyst particles. The introduction of various magnetic nanoparticles such as magnetite, maghemite, ferrites, *etc.* into the photocatalyst matrix has recently become an area of intense research because it allows for the easy separation of the photocatalyst from the treated water using an external magnetic field. Herein, we discuss the recent developments in terms of synthesis and photocatalytic properties of magnetically separable nanocomposites towards water treatment. The influence of the magnetic nanoparticles in the optical properties, charge transfer mechanism, and overall photocatalytic activity is deliberated based on selected results. We conclude the review by providing summary remarks on the successes of magnetic photocatalysts and present some of the future challenges regarding the exploitation of these materials in water treatment.

Keywords: magnetically separable; ferrites; recyclable photocatalysts; photocatalysis; nanocomposites

1. Introduction

Rapid development in terms of industrialisation and population growth over the years has put pressure on sustainable clean water supply. This is partly due to the ever increasing demand and the significant contribution towards compromised fresh water quality that comes with population growth and industrialisation. Similarly, climate change (drought conditions and elevated temperatures) has also impacted negatively on the amount of fresh water available. Consequently, the development of effective water treatment technologies remains an important area of research. This would ensure adequate utilisation of the available fresh water sources, which are constantly polluted through various domestic and industrial activities. Moreover, it would allow efficient treatment of industrial effluent water and enable it to be recycled which would lessen the burden on constant fresh water supply. This is particularly key to the smooth operations of the industries in water scarce localities where the amount of fresh water allocated per industry per day is highly restricted [1].

Over the years, a number of water treatment technologies such as membrane processes [1,2], biological methods [3,4], advanced oxidation processes (AOPs) [5,6], adsorption [7,8], electrochemical

methods [9,10], *etc.* have been developed and explored for the destruction/removal of organic, inorganic, and microbial pollutants. These methods have also been explored in various combinations in order to improve their efficiency [11–14]. Despite the impressive level of success observed with these technologies in water treatment, they often suffer a number of setbacks, which relate to inefficiency, high operational costs, or both. For example, in membrane processes, fouling (organic, inorganic and biofouling) is a major problem that results in the alteration of the membrane flux and rejection properties [15–17]. Toxicity of the effluent matrix and the non-biodegradable nature of some pollutants often render biodegradation ineffective. Moreover, some of the pollutants may be transformed into more toxic compounds during biological treatment, resulting in secondary pollution [18–20]. The generation of highly concentrated sludge which poses further treatment and disposal challenges is a major setback associated with adsorption and coagulation–flocculation [21].

Advanced oxidation processes such as ozonation, hydrogen peroxide oxidation, and their combination with UV light have been extensively exploited in water treatment; however, problems such as the short half-life of ozone, activation by UV light, incomplete mineralisation of organic compounds, and the costs associated with these tools are usually cause for concern [12,22]. Semiconductor photocatalysis has rapidly emerged as the most attractive AOP in recent years for the destruction of organic, inorganic, and microbial pollutants due to a number of advantages it bears over other water treatment protocols. Such merits include its versatile nature in terms of the type of pollutants that can be removed (organic, inorganic, and microbial) and the medium in which the process is applicable (liquid and aqueous medium) [23–27]. Moreover, the semiconductor photocatalysts can also be exploited in other applications such as sensors [28], solar cells [29], pollutant adsorption [30], catalysts for organic synthesis [31], water splitting [32], *etc*. Apart from its versatile nature, semiconductor photocatalysis has the potential to completely mineralise organic pollutants into carbon dioxide, water, and inorganic ions, thereby eliminating the problem of sludge formation which otherwise cause secondary pollution. Semiconductor photocatalysis provides a stable reaction site/medium since the photocatalyst is not used up during the process and can be re-used several times, and the toxicity of some of the pollutants or their matrices does not affect their destruction by photocatalysis as would be the case with biodegradation [33,34]. In addition, photocatalysis has the advantage of being applicable at ambient conditions (room temperature and standard pressure).

Despite all the highlighted merits associated with semiconductor photocatalysis for water treatment, practical exploitation of this technology has remained a daunting challenge. The first challenge relates to the size of the band gap of the semiconductor since this determines the photoresponse of the photocatalyst. Some of the widely exploited semiconductors such as TiO_2, ZnO, SnO_2, *etc.* have wide band gaps of 3.0–3.2, 3.2, and 3.5 eV, respectively, which means these semiconductors can only be activated by UV light irradiation. However, artificial UV sources are costly, and UV light itself is toxic and requires protective gear when working under it. The sun does supply UV light but it only makes up about 4% of the solar spectrum, making practical exploitation unsustainable [35,36]. The second challenge in semiconductor photocatalysis is the fast recombination rate of the photogenerated charge carriers, which ultimately lowers the photocatalytic activity of the semiconductor [37,38]. Ideally, subsequent to light absorption and electron excitation in the semiconductor, the electrons, which are promoted to the conduction band, and the positive holes, which remain in the valence band of the semiconductor, must remain far apart so that they can react with oxygen and water or hydroxide ions to form the superoxide and hydroxyl radicals, respectively. These are the active species that together with the holes may be responsible for the degradation of the pollutants [39,40]. Thirdly, the slow degradation kinetics also hamper the full exploitation of photocatalysis in water treatment. The residence times are usually long and sometimes accompanied by low degradation efficiencies [41]. Incomplete mineralisation of organic pollutants is another problem usually observed in photocatalytic experiments and may lead to the formation of toxic by-products which are more toxic than the parent compound [42]. Lastly, the photocatalysts are usually applied in powdered form, which may undergo aggregation in the aqueous medium thereby

lowering its activity. Moreover, after the treatment has been completed, the photocatalyst needs to be separated and recovered from the water, and this presents an expensive and time-consuming exercise, especially when it comes to nanometre-sized particles. This often leads to inefficient recovery of the photocatalyst, which not only affects its recyclability but also causes secondary pollution and escalates the treatment costs.

Over the past years, tremendous work has been done focusing on improving the visible light response of various photocatalysts, enhancing charge carrier separation and the overall photocatalytic activity. Efficient utilisation of visible light would enable the exploitation of sunlight as a source of energy, which consists of about 40% visible light. Generally, strategies such as doping the semiconductor with metal ions (alkali, alkaline earth, noble, rare earth, and transition metals) [43–47], non-metal ions (oxygen, sulphur, nitrogen, phosphorus, halogens, carbon, and boron) [48–51], codoping/multidoping (metal + metal, non-metal + metal, non-metal + non-metal) [52–55], coupling semiconductors with carbon nanomaterials (reduce graphene oxide (RGO), graphene oxide (GO), multiwalled carbon nanotubes (MWCNTs), single-walled carbon nanotubes (SWCNTs), carbon nanospheres (CNS), fullerenes, *etc*.) [56–59], sensitisation (dye, polymer and surface complex sensitisation) [60–62], and coupling two or more semiconductors [63–65] have been extensively investigated for improving the photocatalytic activity of various semiconductors. Encouraging results have been reported, especially for the nanocomposite photocatalysts, which showed improved visible light utilisation and efficient charge separation, which could be ascribed to the combined contribution of the individual components of the nanocomposite.

Engineering of materials with high visible light photocatalytic activity that are easily separable and recoverable from the treated water remains the ultimate goal of ongoing research. With the increased usage of nanophotocatalysts, efficient separation and recovery of these materials from water is becoming increasingly difficult. Immobilising the photocatalyst particles on solid supports such as glass, ceramics, polymers, zeolites, sand, *etc.* has been widely investigated and has successfully enabled easy separation of the photocatalyst [66–71]. However, in the process of attaining easy separation, the photocatalytic activity of the immobilised semiconductors decreased remarkably. This was due to a decrease in the surface area, poor interaction with the reaction medium, and limited exposure of the photocatalyst to light [72,73]. Since neither the photocatalytic activity nor the easy separation can be sacrificed, researchers turned their interests to magnetic nanoparticles as integral ingredients for developing photocatalysts, which were easily separated from water with an external magnetic field [74–76]. Magnetic nanoparticles such as haematite (α-Fe_2O_3), maghemite (γ-Fe_2O_3), magnetite (Fe_3O_4), ferrites (MFe_2O_4, M = Mg, Ni, Zn, Cu, Co, Cd, *etc*.), *etc.* have been successfully coupled with various photocatalysts to induce magnetic behaviour in the composite material and allow easy magnetic separation [39,77–79]. Since the photocatalyst remains powdery upon incorporation of the magnetic nanoparticles, this does not compromise its surface area and the distribution of the photocatalyst in the aquatic medium. In addition, some of these magnetic nanoparticles have good visible light absorption and photocatalytic properties, which further enhance the overall pollutant degradation kinetics over the magnetic nanocomposite [39,40,64,80–82].

Considering the future prospects of magnetic photocatalysts, the design and preparation of magnetic visible-light-active nanocomposites has emerged as a hot topic in photocatalytic environmental pollution control. Therefore, it is necessary to bring into perspective the current developments in the tailoring and application of such materials in water treatment. A few reviews are available mainly on the synthesis, structure, and various applications of magnetic materials [83–88]. This review exclusively discusses the most recent developments in terms of the synthesis and exploitation of various magnetic nanocomposite photocatalysts in water pollution mitigation. Details on the synthesis routes and structure of the various magnetic nanoparticles have been well-reviewed and have been excluded in this review. Furthermore, this review only focusses on iron oxide magnetic nanoparticles resulting in four categories of magnetic nanocomposite photocatalysts: haematite, maghemite, magnetite, and ferrite-based magnetic photocatalysts. Under each category, we discuss the

influence of the magnetic nanoparticle on optical properties, charge transfer mechanism, and the overall photocatalytic properties of the nanocomposites. We conclude the review by providing some summary remarks and highlight the future challenges towards tailoring and utilising magnetic photocatalysts in water treatment.

2. Recent Developments in Magnetic Photocatalysts

2.1. Haematite (α-Fe_2O_3)-Based Magnetic Photocatalysts

As a pristine material, haematite is a narrow band gap semiconductor (2–2.2 eV) with good visible light response, good chemical stability, low-cost, ferromagnetic behaviour, abundantly available, high resistance to corrosion, and environmentally friendly [89–91]. On its own, haematite shows poor photocatalytic activity due to the high recombination rate of the charge carriers and poor conductivity [90,91]. Despite its poor photocatalytic activity, the narrow band gap of haematite makes it an ideal sensitiser for improving the visible light response of various semiconductors. Zhao *et al.* developed a nanostructured α-Fe_2O_3-AgBr nonwoven cloth (Figure 1a,b) via a simple electrospinning-calcination method and studied its visible light photocatalytic behaviour towards rhodamine B (RhB) and para-chlorophenol (4-CP) decomposition. For both pollutants, the α-Fe_2O_3-AgBr nonwoven cloth showed superior activity over α-Fe_2O_3 and AgBr clothes individually, attaining 91.8% 60 min and 74.2% in 120 min for RhB and 4-CP decomposition, respectively [81]. Coupling AgBr with α-Fe_2O_3 resulted in a significant red-shift and resulted in the formation of heterojunctions, which facilitated charge separation, thereby improving the overall photocatalytic activity of the α-Fe_2O_3-AgBr nonwoven cloth. In addition, the cloth was easy to handle and recycle during photocatalysis by simple dipping and removal or by using an external magnet. It was found that the composite cloth was stable over four cycles with only a slight decrease in photocatalytic performance [81].

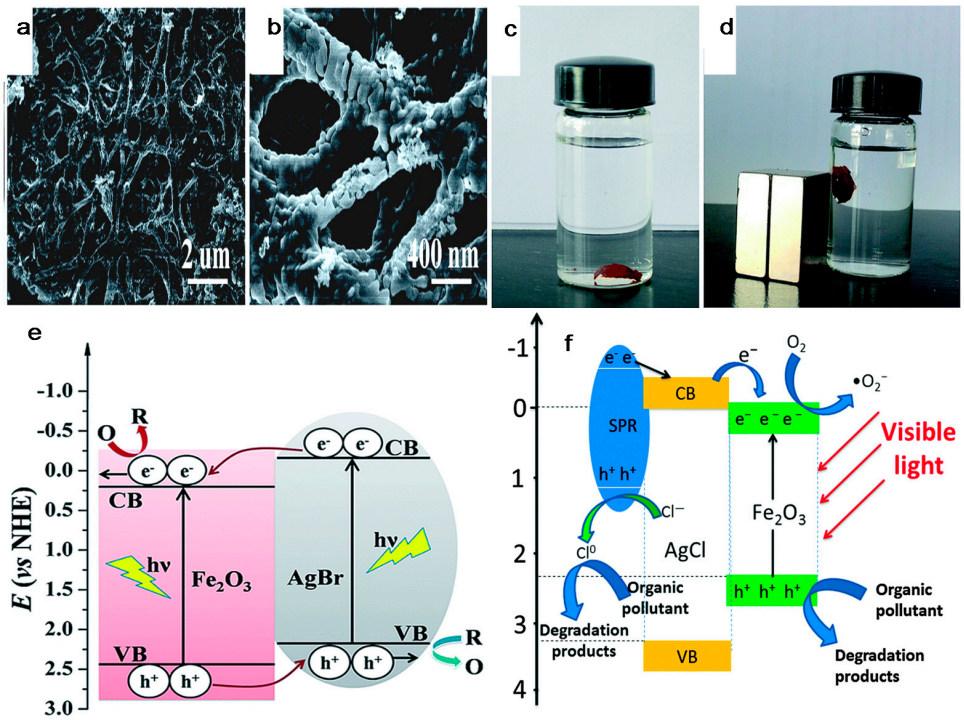

Figure 1. (**a**,**b**) SEM images of α-Fe_2O_3-AgBr nonwoven cloth; (**c**,**d**) illustration of magnetic separation of α-Fe_2O_3-AgBr cloth and charge transfer mechanism in (**e**) α-Fe_2O_3-AgBr cloth (Reproduced with permission from [81], Copyright 2015, RSC); and (**f**) Ag/AgCl/Fe_2O_3. Reproduced with permission from [39]. Copyright 2016, RSC.

Xue and coworkers fabricated magnetically separable α-Fe_2O_3/graphitic carbon nitride (g-C_3N_4) nanocomposite photocatalysts with varying α-Fe_2O_3 loadings (5%, 10%, 30%, 50%) and investigated their performance for degradation of RhB. The highest degradation efficiency (96.7% in 4 h) was recorded using the sample containing 10% α-Fe_2O_3, which suggests optimum composition [92]. The introduction of α-Fe_2O_3 nanoparticles into g-C_3N_4 matrix enhanced its visible light utilisation and charge separation efficiency. Moreover, the composite photocatalyst displayed good stability and could be easily separable and recycled using an external magnet [92]. Similarly, core-shell magnetically separable Ag/AgCl/Fe_2O_3 showed remarkable photocatalytic activity towards bisphenol A (BPA) and *E. coli* under visible light exposure. At a 5% α-Fe_2O_3 loading, the composite photocatalyst reached the highest activity, which was 13 times that of Ag/AgCl for BPA degradation, and complete destruction of *E. coli* was observed after just 30 min of irradiation [39]. The nanocomposite displayed good stability and sufficient magnetic response to an external magnet.

In terms of charge transfer mechanism, the path followed by the electrons and holes depends on the semiconductor coupled with haematite and how their band structures match. In any case, under visible light illumination, haematite is excited and electrons accumulate in the conduction band while leaving positive holes in the valence band. In the case of α-Fe_2O_3-AgBr, both semiconductors are excited by visible light, and the electrons from AgBr transfer to the conduction band of α-Fe_2O_3, while the holes transfer in the opposite direction (Figure 1e). The holes will directly attack the organic pollutants to form the degradation products, while the electrons may react with adsorbed oxygen leading to the eventual formation of hydroxyl radicals, which are strong oxidising agents [81]. In the Ag/AgCl/Fe_2O_3 ternary nanostructure, the charge transfer mechanism (Figure 1f) is a bit complex. Only Ag and α-Fe_2O_3 are excited upon visible light absorption, and the plasmon-generated electrons in Ag will be injected into the conduction band of AgCl and further transfer to the conduction band of α-Fe_2O_3. Meanwhile, the holes in α-Fe_2O_3 can directly decompose the pollutants, while the holes left in Ag react with Cl^- ions to form Cl^0, which then attacks the pollutants [39].

Other haematite-based magnetically separable nanostructured photocatalysts such as graphene (GR)-α-Fe_2O_3-ZnO [93], α-Fe_2O_3/TiO_2 nanofibres [94], α-Fe_2O_3/RGO [95], and α-Fe_2O_3/ZnO [96] have been fabricated, have shown remarkable visible light utilisation, and have been easily separable using an external magnetic field. Coupling the various semiconductors with α-Fe_2O_3 resulted in synergy between the materials, leading to enhanced visible light response, improved charge separation, and an overall increase in photocatalytic activity. Moreover, the incorporation of haematite allowed for the easy separation of the photocatalysts after the water treatment. However, α-Fe_2O_3 generally shows weak ferromagnetic behaviour, and, most importantly, its magnetic properties largely depend on the synthesis method, which influences its particle size and shape [92]. Several α-Fe_2O_3-incorporating heterostructures such as α-Fe_2O_3/Ag_3VO_4 [91], g-C_3N_4/Ag/α-Fe_2O_3 [97], g-C_3N_4/α-Fe_2O_3 [98–100], α-Fe_2O_3/TiO_2 [101] Au/g-C_3N_4/α-Fe_2O_3 [102], and α-Fe_2O_3/CdS [90] have been fabricated, showing enhanced visible light photocatalytic properties, and no magnetic behaviour was reported. Therefore, when the main aim of incorporating the iron oxide nanoparticles is to induce magnetic response, haematite may not be the ideal choice.

2.2. Maghemite (γ-Fe_2O_3)-based Magnetic Photocatalysts

Maghemite is another important form of iron oxide but, unlike haematite, it shows good magnetic properties with saturation magnetisation values of up to 76 emu/g [103]. Consequently, the incorporation of maghemite into various photocatalyst matrices has been explored to fabricate magnetically separable composite photocatalysts for easy recovery and recycling [104,105]. Interestingly, despite the sensitivity to an external magnetic field, when the magnetic field is removed, the γ-Fe_2O_3-incorporating nanocomposites do not retain any significant residual magnetism that would otherwise cause problems by creating large clusters of magnetised particles during water treatment [106]. Maghemite shows good visible light response owing to its narrow band gap (2.2 eV) and possesses good adsorption properties. However, its photocatalytic activity is poor as a result

of the high recombination rate of the photogenerated charge carriers and photodissolution [74,107]. Two approaches are usually adopted when coupling maghemite with other semiconductors. In the first approach, maghemite is directly coupled with other semiconductors to form heterojunctions, and it contributes towards visible light response of the nanocomposite photocatalyst as well as the overall charge transfer process [74,108,109]. According to the second approach, maghemite and the other semiconductor do not form heterojunctions (not in direct contact), but they are separated by an inert layer or shell usually silica (SiO_2). This is aimed at preventing photodissolution of the iron oxide and charge transfer between the two materials, which could otherwise result in the recombination on the maghemite surface. In this case, maghemite nanoparticles do not play any part in the photocatalysis process but function solely in the magnetic separation of the photocatalyst from the reaction medium [104,106,110].

A magnetically separable quaternary γ-Fe_2O_3/N and Fe-codoped TiO_2 nanocomposite was prepared using a sol-gel method (as illustrated in Figure 2a) and employed for the decomposition of reactive blue 4 (RB 4) under visible light illumination. Significantly higher photocatalytic activity was observed over the quaternary nanocomposite photocatalyst compared to N,Fe-TiO_2, N-TiO_2, and TiO_2, reaching 100% degradation in 180 min (Figure 2b) [111]. The remarkable improvement in activity of the nanocomposite could be explained in terms of the combined contribution of codoping TiO_2 and coupling with γ-Fe_2O_3, which resulted in significant band gap narrowing, efficient visible light response, and efficient charge separation and transfer. Furthermore, the multicomponent photocatalyst demonstrated good stability and recyclability over four cycles without any significant loss in activity or magnetic properties, which allowed for easy magnetic separation [111]. Yu and coworkers probed the adsorption and UV photocatalytic oxidation of As(III) over TiO_2 decorated on magnetic (γ-Fe_2O_3) mesoporous SBA-15 nanocomposite (γ-Fe_2O_3/SBA-15/TiO_2) derived from simple inner-pore hydrolysis combined with solvent evaporation route [112]. The nanocomposite photocatalyst displayed a dual function of adsorption and photocatalytic degradation. Firstly, As(III) ions were adsorbed onto the photocatalyst and then upon UV irradiation, undergo photocatalytic oxidation to As(V), which is less toxic and also removable by the photocatalyst. In addition, the photocatalyst showed good stability and could be regenerated for five cycles using NaOH (0.01 M) and still maintained over 90% As(III) removal and good magnetic properties for easy separation [112]. The incorporation of the SBA-15 ensured good dispersibility of the nanoparticles and improved the surface area of the nanocomposite. All three components of the nanocomposite were equally important in the overall removal of As(III).

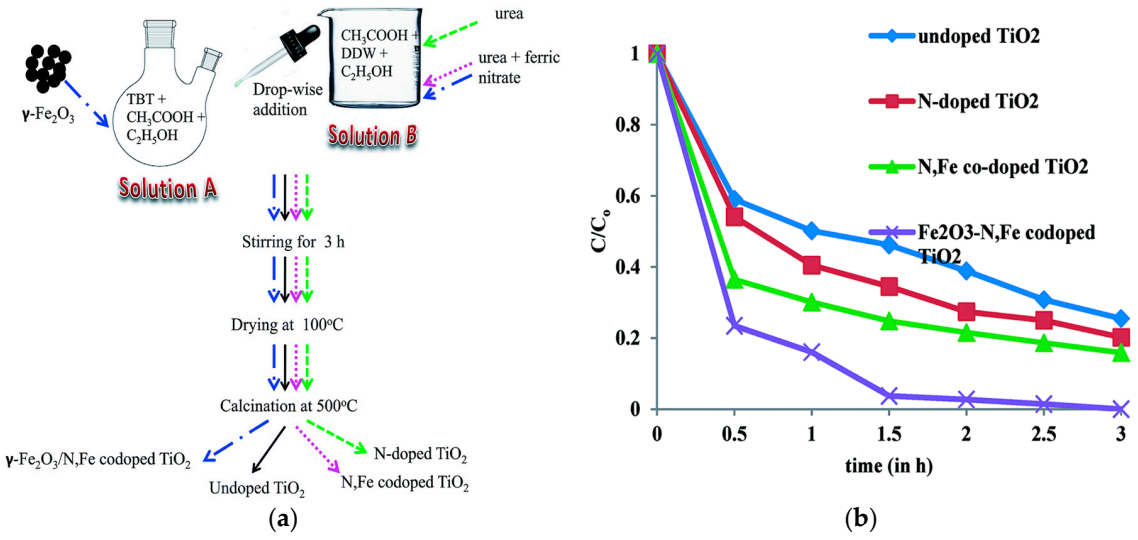

Figure 2. (**a**) Schematic illustration of the sol-gel preparation of γ-Fe_2O_3/N.Fe-TiO_2; and (**b**) photocatalytic degradation of RB 4 over γ-Fe_2O_3/N.Fe-TiO_2 and the controls. Reproduced with permission from [111]. Copyright 2015, RSC.

Improved optical and photocatalytic properties have also been reported for other magnetic photocatalysts such as ZnO/γ-Fe_2O_3 [113], g-C_3N_4/γ-Fe_2O_3 [109], and γ-Fe_2O_3/TiO_2 [74] towards the degradation of various pollutants including RhB, methylene blue (MB), and methyl orange (MO). Moreover, these nanostructures showed good stability and could be magnetically separated and recycled without a significant loss in activity. However, the maghemite nanoparticle loading needs to be carefully controlled in order to strike a good balance between sufficient magnetism to facilitate separation and the detrimental effect of recombination of the charge carriers on the maghemite nanoparticles. This means that, while enjoying the luxury of easy separation, the detrimental effect of recombination must not be ignored in order to positively benefit from the incorporation of the maghemite nanoparticles.

According to the proposed charge transfer route in γ-Fe_2O_3/N,Fe-TiO_2 (Figure 3a), both maghemite and codoped titania absorb visible light, and electrons are excited from the valence band to the conduction band in γ-Fe_2O_3, leaving holes in the valence band. Similarly, in the codoped titania, electrons are excited from the valence band of TiO_2 to the impurity states formed by Fe doping and also from N sub-band gap states to the conduction band of TiO_2. Subsequently, electrons transfer from the conduction band of maghemite to the Fe impurity states in TiO_2, while the holes migrate to the N states in TiO_2. The electrons and holes will be captured by molecular oxygen and water to form the superoxide and hydroxyl radicals, respectively [111]. These radical species are important oxidising agents for pollutant decomposition.

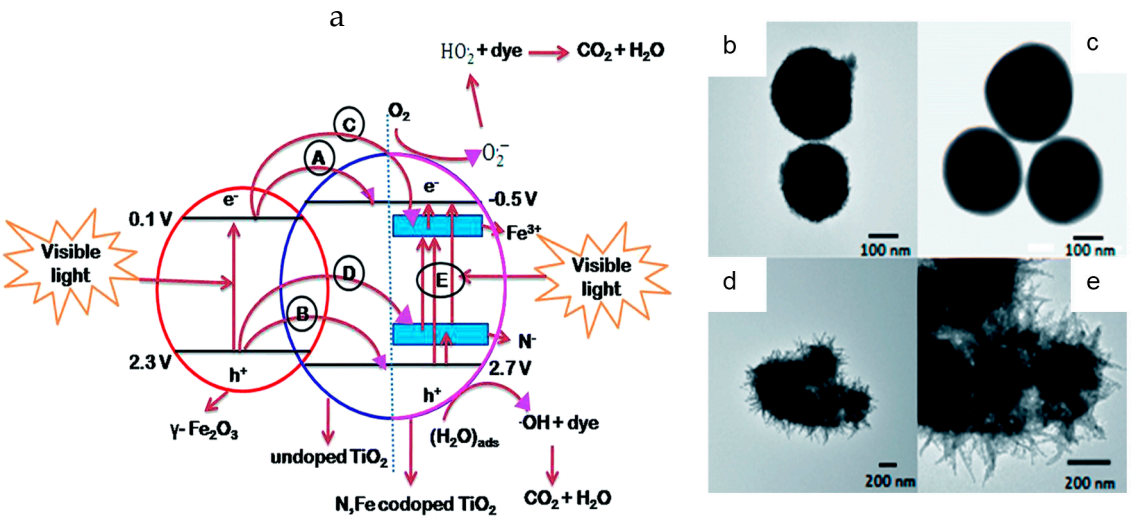

Figure 3. (**a**) Charge transfer mechanism in γ-Fe_2O_3/Fe,N-TiO_2 (Reproduced with permission from [111], Copyright 2015, RSC) and (**b**–**e**) SEM images of urchin-like γ-Fe_2O_3@SiO_2@TiO_2 composite microparticles. Reproduced with permission from [114]. Copyright 2015, RSC.

The strategy of preventing the formation of heterojunctions between maghemite and the semiconductor coupled with it has been widely explored using silica as the barrier/shell surrounding the magnetic core. For example, Szeto *et al.* used a layer-by-layer assembly route to fabricate urchin-like γ-Fe_2O_3@SiO_2@TiO_2 composite microparticles (Figure 3b–e) and observed enhanced phenol decomposition under UV irradiation [114]. The tailored composite photocatalyst was shown to possess a large surface area, a prolonged life of the charge carriers, remarkable permeability, and significantly higher photocatalytic activity compared to commercial P25. In addition, incorporation of the maghemite nanoparticles ensured easy and efficient separation of the photocatalyst using an external magnetic field [114]. Similar results have been reported for other magnetic heterostructures such as γ-Fe_2O_3@SiO_2@Ce-TiO_2 [110], γ-Fe_2O_3@SiO_2@AgBr:Ag [104], and γ-Fe_2O_3@SiO_2@TiO_2 [106], whereby a silica coating separates the maghemite nanoparticles from direct contact with the other components of the heterostructure. In these nanocomposites, the maghemite nanoparticles were only

incorporated to facilitate the magnetic separation and play no part in the charge transfer process and overall photocatalytic decomposition of the pollutants. Although this approach is logical and has yielded some positive results, a critical comparison between the heterojunction type of photocatalyst and the core-shell structure of the same nanocomposite is rarely documented. This could map a way forward in terms of the most efficient approach towards engineering the maghemite-based magnetic photocatalyst and benefitting from the properties of this material.

2.3. Magnetite (Fe_3O_4)-based Magnetic Photocatalysts

Magnetite is by far one of the most widely exploited iron oxide magnetic nanoparticle in the fabrication of magnetic photocatalysts due to its low toxicity, good magnetic properties, biocompatibility, and remarkable adsorption properties [115,116]. The magnetisation saturation for magnetite can reach values of up to 92 emu/g, making it the ideal candidate for synthesis of magnetically separable photocatalysts [103]. However, unlike maghemite, magnetite shows no photocatalytic properties, and, like maghemite, the formation of heterojunctions with other semiconductors in nanocomposite photocatalysts is undesirable because magnetite may suppress the overall photocatalytic efficiency by acting as a recombination centre for the charge carriers [117,118]. Silica is commonly utilised to enclose the magnetite core, which is wrapped with the other semiconductor nanoparticles to form the magnetic composite photocatalysts. The silica barrier prevents electron transfer between magnetite and the other semiconductor, additionally preventing photodissolution of the iron oxide [119,120].

Despite the possible negative effect of magnetite in heterojunction nanocomposites, several reports on successful tailoring and improvement in photocatalytic activity over heterojunction nanocomposites have emerged, and careful control of the Fe_3O_4 loading in the nanocomposite is an important point of consideration. For example, Zhao *et al.* observed enhanced photocatalytic activity towards ampicillin (AMP) over $Fe_3O_4/TiO_2/Ag$ with a sea urchin-like morphology, both under visible and UV light irradiation. The composite photocatalyst reached 98.7% and 91.5% AMP degradation after 360 min of UV and visible light illumination, respectively [116]. Furthermore, the nanocomposite possessed good magnetic behaviour with a magnetisation saturation of 26.5 emu$\cdot g^{-1}$ (Figure 4), which was high enough to facilitate magnetic separation (Figure 4 insert). In addition to the degradation of AMP, the nanocomposite photocatalyst showed remarkable photocatalytic properties towards *S. aureus* (G^+), *E. coli* (G^-), and *A. niger* [116]. In another example, improved MO decomposition was realised over Fe_3O_4/N-TiO_2/Ag hollow nanospheres, reaching 99.5% in 80 min of visible light exposure when the Ag loading was 1.0% [121]. Ma and coworkers employed a low-temperature crystallisation method to wrap Fe_3O_4 spheres with TiO_2 nanoparticles and subsequently immobilised Au nanoparticles on the core-shell Fe_3O_4/TiO_2 to yield a Fe_3O_4/TiO_2/Au plasmonic magnetic photocatalyst. RhB was used as a model pollutant to evaluate the photocatalytic properties of the nanocomposite, and it showed superior performance over Fe_3O_4 and Fe_3O_4/TiO_2, with good magnetic properties (magnetisation saturation (Ms), 44.6 emu$\cdot g^{-1}$), and recyclability [122]. The heterojunctions formed between Fe_3O_4 and titania allow electrons to transfer between the two materials, which improves charge separation. However, the Fe_3O_4 loading needs to be kept in check as excess Fe_3O_4 will cause detrimental effects. Therefore, Fe_3O_4 nanoparticles have a dual function in the heterojunction nanostructures—electron trapping and enabling magnetic separation.

Li *et al.* fabricated Fe_3O_4 magnetic core coated with SiO_2 prior to the deposition of TiO_2 and surface modification with lysine, and the quaternary nanocomposite photocatalyst (Fe_3O_4@SiO_2@TiO_2-lysine) showed multifunctional properties as it was employed as an adsorbent, photocatalyst, and sensor for dissolved organic and inorganic phosphorus in seawater [123]. The photocatalyst displayed remarkable stability and could be magnetically separated and recycled for 10 cycles without any significant loss in its adsorption and photocatalytic properties [123]. Other core-shell Fe_3O_4@SiO_2 nanostructures decorated with TiO_2 have been fabricated and evaluated for the decomposition of various pollutants such as RhB, 2-chlorophenol (2-CP), phenol, MB, and MO. These materials showed

improved photocatalytic properties, good stability, and sufficiently high magnetic response that enabled separation using an external magnetic field [124–127]. Table 1 provides a summary of the synthesis and photocatalytic properties of various other magnetite-incorporating titania-based photocatalysts towards water treatment applications. In the magnetic core-shell nanostructures, the Fe_3O_4 nanoparticles encapsulated with the silica shell do not partake in the charge transfer process but only in the magnetic separation of the photocatalyst.

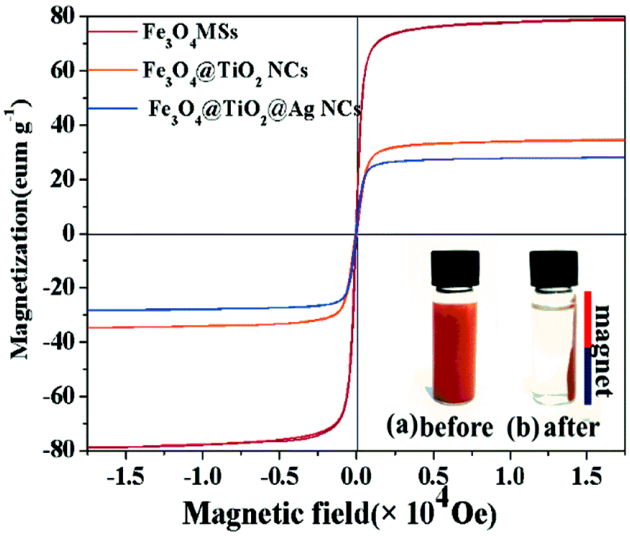

Figure 4. Magnetization curves and insert showing magnetic separation of $Fe_3O_4/TiO_2/Ag$. Reproduced with permission from [116]. Copyright 2016, RSC.

Table 1. Summary of the photocatalytic properties of Fe_3O_4-incorporating TiO_2-based photocatalysts.

Sample	Preparation Method	Application	Catalyst Dose	Pollutant Concentration	Degradation Efficiency	Saturation Magnetisation	Reference
Fe_3O_4/GO/Ce-TiO_2	Low-temperature sol-gel/ ultrasonication	Degradation of tetracycline (TC)/Vis/300 W Xe lamp/400 nm UV filter	0.050 g	25 ppm	82.9% in 60 min	No data	[33]
Fe_3O_4/RGO/TiO_2	Reduction-deposition	Degradation of MB and tetrabromobisphenol A (TBBPA)/UV/230 W Hg lamp	0.025 g	10 ppm	99.5% in 60 min/TBBPA, 95.9% in 60 min/MB	1.14 emu/g	[128]
Fe_3O_4/P(MAA-DVB)/TiO_2	Magnetic field induced assembly/precipitation-polymerisation	Degradation of RhB/UV/250 W Hg lamp	0.040 g	4.43 ppm	71.5% in 120 min	35.2 emu/g	[129]
Fe_3O_4@SiO_2@N-TiO_2	Sol-gel	Degradation of phenol/Vis/15 W florescent lamp	0.800 g	100 ppm	46% in 480 min	~2 emu/g	[127]
Fe_3O_4/chitosan/TiO_2	Hydrothermal/crosslinking	Degradation of MB/UV/8 W UV lamp	1.00 g	1.28 ppm	93% in 40 min	4.2 emu/g	[130]
Fe_3O_4/TiO_2	Reverse microemulsion/sol-gel	Degradation of RhB/UV/50 W Xe lamp	0.004 g	22.12 ppm	100% in 100 min	21.68 emu/g	[131]
Ag_3PO_4/TiO_2/Fe_3O_4	*In situ* hydrolysis/deposition	Degradation of acid orange 7 (AO 7)/50 mW diode blue laser and *E. coli*/Vis/300 W Xe lamp/420 nm UV filter	0.100 g	5.25 ppm/AO7 and 10^7 CFU/mL/*E. coli*	~100% in 2.5 min/AO 7, 99.8% in 5 min/*E. coli*	No data	[38]
Fe_3O_4/TiO_2/Bi_2O_3	Sol-gel	Degradation of MO/Simulated solar light/350 W Xe lamp	0.200 g	No data	69% in 150 min	No data	[132]
Fe_3O_4/TiO_2/Au	Sol-gel/hydrothermal	Degradation of MB and *E. coli*/UV/4 × 9 W black lights	0.015 g/MB and 0.010 g/*E. coli*	8.00 ppm/MB and 10^8 CFU/mL/*E. coli*	78% in 4 h/MB, 89.3% in 60 min/ *E. coli*	No data	[133]
Ag@Fe_3O_4@SiO_2@TiO_2	Solvothermal	Degradation of MB and Cr(VI) reduction/Vis/500 W Xe lamp/ 425 UV filter	0.020 g	50 ppm/MB and 22.24 ppm/$K_2Cr_2O_7$	99.9% in 4 h/ Cr(VI), ~90 mg/g/MB	13.92 emu/g	[134]
Fe_3O_4@SiO_2@TiO_2@GO	Reverse microemulsion/sol-gel/amide conjugation	Degradation of RhB/UV/400 W column high pressure Hg lamp	0.050 g	8.85 ppm	92% in 120 min	16.90 emu/g	[120]
Fe_3O_4@C@TiO_2	Solvothermal/calcination	Degradation of RhB/UV/125 W high pressure Hg lamp	0.020 g	10 ppm	~100% in 80 min	6.04 emu/g	[135]

Table 1. *Cont.*

Sample	Preparation Method	Application	Catalyst Dose	Pollutant Concentration	Degradation Efficiency	Saturation Magnetisation	Reference
Fe_3O_4@SiO_2@TiO_2	Stobber process/sol-gel/chemical precipitation	Degradation of RhB/UV/50 W high pressure Hg lamp	0.010 g	8.85 ppm	100% in 10 min	30.60 emu/g	[136]
Fe_3O_4/TiO_2	Hydrothermal	Degradation of MB/UV/9 W UV lamp	0.002 g	1.00 ppm	100% in 10 min	No data	[75]
Fe_3O_4@TiO_2@GR	Sol-gel/assembly route	Degradation of 2,4-dichlorophenoxy-acetic acid (2,4-D)/simulated solar light/ 500 W Xe arc lamp	0.020 g	20 ppm	100% in 40 min	13.00 emu/g	[137]
WO_3/TiO_2/Fe_3O_4	Sol-gel	Degradation of direct blue 71 (DB 71)/Vis/200 W Xe lamp	0.030 g	50 ppm	98% in 35 min	18.20 emu/g	[138]

Chidambaram and coworkers prepared a novel plasmonic, magnetic Fe_3O_4/ZnO/Ag nanocomposite and employed it for the photocatalytic degradation of MB under visible light illumination. Complete MB removal was observed after 6 h of visible light exposure on Fe_3O_4/ZnO/Ag, while only 20% MB removal was realised over Fe_3O_4/ZnO during the same irradiation time. The improved activity could be explained in terms of improved charge separation and the surface plasmon resonance (SPR) effect of Ag nanoparticles, which is responsible for the visible light activity of the nanocomposite photocatalyst [139]. Fe_3O_4 nanoparticles played a dual role of facilitating charge separation and enabling magnetic separation. In addition, the photocatalyst showed great stability over 10 cycles without much loss in activity or magnetic properties. Upon visible light irradiation, the SPR-generated electrons are injected into the conduction band of ZnO and further transfer to the Fe_3O_4 nanoparticles. Subsequently, the electrons reduce Fe^{3+} to Fe^{2+}, which in turn is oxidised back to Fe^{3+} upon reaction with adsorbed oxygen forming the superoxide radicals. Meanwhile, the SPR-generated holes in Ag could react with water to form the hydroxyl radicals and together with the superoxide radicals are responsible for pollutant degradation [139]. Yan *et al.* observed higher visible light photocatalytic performance over urchin-like Fe_3O_4@SiO_2@ZnO/CdS core-shell microspheres (Figure 5a,b) towards RhB compared to Fe_3O_4@SiO_2@ZnO microspheres. Coating Fe_3O_4 with SiO_2 prevented the formation of heterojunctions with ZnO and CdS, and the nanocomposite showed good magnetic properties with magnetisation saturation value of 18.97 emu/g [140]. On visible light exposure, only CdS nanoparticles were excited and played the role of a sensitiser for ZnO, with electrons transferred to the conduction band of ZnO while the holes remained in the valence band of CdS (Figure 5c), resulting in efficient charge separation and the formation of the oxidising species [140].

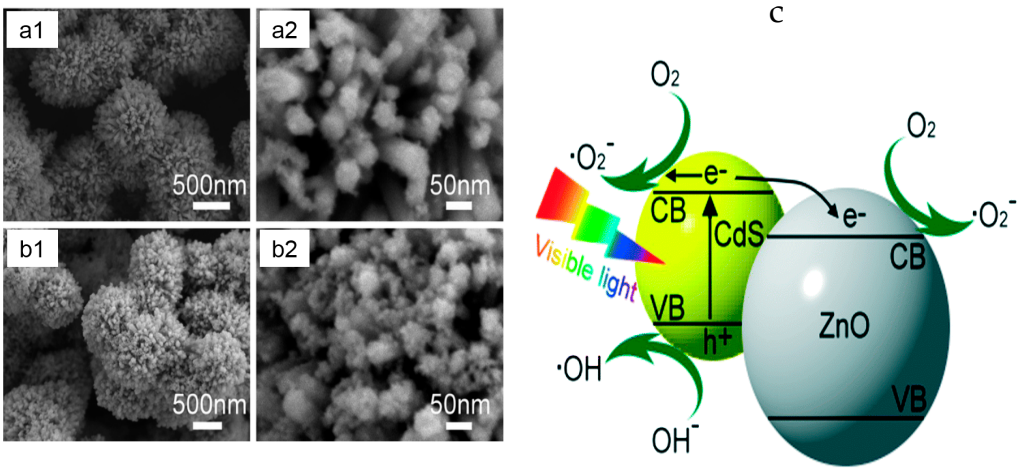

Figure 5. (**a**,**b**) SEM images of urchin-like Fe_3O_4@SiO_2@ZnO/CdS microspheres and (**c**) charge transfer route in Fe_3O_4@SiO_2@ZnO/CdS. Reproduced with permission from [140]. Copyright 2016, RSC.

Habibi-Yangjeh's group has recently prepared and investigated the visible light photocatalytic properties of various magnetic nanocomposites-based on Fe_3O_4 and ZnO such as ZnO/AgI/Fe_3O_4 [141], ZnO/AgBr/Fe_3O_4/Ag_3VO_4 [142], ZnO/Ag_3VO_4/Fe_3O_4 [143], Fe_3O_4/ZnO/AgCl [144], and Fe_3O_4/AgBr-ZnO [145] towards model pollutants such as RhB, phenol, MB, and MO. All of the nanocomposite photocatalysts showed good photocatalytic properties, which can be credited to efficient charge separation and improved visible light absorption as a result of the heterojunctions formed between ZnO and the co-catalysts. Moreover, it was shown that despite the formation of the composite photocatalysts, the presence of Fe_3O_4 nanoparticles ensured that the photocatalysts still retained sufficient magnetic response to allow for efficient separation using an external magnetic field. Obviously, the magnetisation saturation of Fe_3O_4 decreased sharply upon the formation of the nanocomposites due to their interaction and coverage by the non-magnetic components of the photocatalysts [141–145]. Under visible light irradiation, ZnO remains inactive

and only the co-catalyst with a narrow band gap can be excited. For example, in ZnO/AgI/Fe_3O_4 and ZnO/AgBr/Fe_3O_4/Ag_3VO_4, only AgI, AgBr, and Ag_3VO_4, respectively, are excited, and electrons are promoted to the conduction band, while the holes remain in the valence band. Subsequently, the electrons transfer to the conduction band of ZnO where they react with adsorbed oxygen to form the radical species (superoxide and hydroxyl radicals). Accordingly, the holes are directly involved in the degradation of the pollutants since they are not positive enough to oxidise water for the hydroxyl radicals [141,142]. The electrons and holes occupied different sites in the nanocomposite photocatalysts, which ensured efficient charge separation and the formation of the reactive species for pollutant degradation.

Owing to its meta-free nature, polymeric structure, non-toxicity, good visible light response, good photocatalytic properties, and high thermal and chemical stability, tailoring graphitic carbon nitride (g-C_3N_4)-based magnetic photocatalysts is an important exploit towards potential practical application of these materials in water treatment. Using a combination of calcination and co-precipitation, Yang and coworkers prepared Fe_3O_4/g-C_3N_4 nanocomposite photocatalyst and probed its photocatalytic behaviour towards 2,4,6-trichlorophenol (2,4,6-TCP) under visible light illumination [77]. In a similar work, Jia *et al.* fabricated Fe_3O_4/g-C_3N_4 via a hydrothermal route and studied its visible light photocatalytic performance towards RhB decomposition [146]. In both studies, higher photocatalytic performance was observed over the nanocomposites compared to Fe_3O_4 and g-C_3N_4 individually, reaching 95.5% in 60 min [146] and 96.5% in 100 min [77] for RhB and 2,4,6-TCP, respectively. Coupling g-C_3N_4 with Fe_3O_4 improved charge separation since only g-C_3N_4 is excited by visible light, and the electrons in the conduction band quickly transfer to Fe_3O_4, where they are captured by oxygen to form the radical species. Meanwhile, the holes remain in the valence band of g-C_3N_4 and directly oxidise the pollutants to form the degradation products. Therefore, the holes and electrons occupy different locations in the nanocomposite. Moreover, magnetic separation was made possible by the presence of the Fe_3O_4 nanoparticles [77,146].

Habibi-Yangjeh's group investigated the visible light photocatalytic performance of novel magnetic nanocomposites: g-C_3N_4/Fe_3O_4/BiOI [147], g-C_3N_4/Fe_3O_4/AgCl [148], and g-C_3N_4/AgBr/Fe_3O_4 [149] towards the decomposition of RhB, MO, and MB. Significantly higher photocatalytic activity was observed over the ternary heterostructures compared to single and binary nanocomposites, and this could be ascribed to the synergistic effect of the various components of the ternary nanocomposites, resulting in improved visible light response and charge separation efficiency. Moreover, the presence of Fe_3O_4 in the heterostructures endowed them with magnetic response, which allowed separation using an external magnetic field [147–149]. In terms of charge transfer, only g-C_3N_4 is excited by visible light in the case of g-C_3N_4/Fe_3O_4/AgCl, while both g-C_3N_4 and BiOI are excited in g-C_3N_4/Fe_3O_4/BiOI, and the electrons are promoted to their conduction bands, leaving positive holes in the valence bands. This is followed by the transfer of electrons from the conduction band of g-C_3N_4, which is more negative, to the conduction bands of AgCl and BiOI, which are less negative, whereby photoreduction reactions involving adsorbed oxygen take place and result in the formation of the radical species [147,148]. Accordingly, in both materials, the holes accumulate in the valence band of g-C_3N_4 where they directly oxidise the pollutants to form the degradation products.

Generally, the incorporation of Fe_3O_4 nanoparticles in the photocatalysts can serve as a means to prolong the life of the photogenerated charge carriers by acting as electron traps and induce magnetic response in the nanocomposites, which enables easy separation using an external magnetic field. In both magnetic core-shell and heterojunction nanostructures, the magnetic influence of the Fe_3O_4 nanoparticles was significant despite showing lower magnetisation saturation compared to neat Fe_3O_4 due to the presence of the non-magnetic components of the photocatalysts. In the heterojunction nanostructures, Fe_3O_4 nanoparticles played a dual role of charge separation and magnetic separation, but the detrimental effect of recombination becomes a problem if the optimum Fe_3O_4 loading is not carefully controlled. Meanwhile, the silica shell in the core-shell nanostructures serve as a barrier to prevent the formation of heterojunctions and charge transfer, limiting the role of the Fe_3O_4 nanoparticles only to magnetic separation of the photocatalysts. A host of other Fe_3O_4-based magnetic photocatalyst have been designed, prepared, and exploited in water treatment applications and are summarised in Table 2.

Table 2. Summary of the photocatalytic properties of various Fe_3O_4-based photocatalyst.

Sample	Preparation Method	Application	Catalyst Dose	Pollutant Concentration	Degradation Efficiency	Magnetisation Saturation	Reference
Fe_3O_4@SiO_2@CdS	Stobber method/chelating assisted growth	Degradation of MB and TC/Vis	0.010 g	10 ppm/MB and 100 ppm/TC	80% in 21 min/TC, 94% in 140 min/MB	22.00 emu/g	[63]
Fe_3O_4(TAMH)/ZnO	Solvothermal	Degradation of phenol/Vis/ 575 W MSR metal halide lamp	0.325 g	20 ppm	71.3% in 150 min	No data	[150]
Fe_3O_4@mSiO_2@BiOBr	Solvothermal	Degradation of MB/Vis/500 W Xe lamp/420 nm UV filter	0.100 g	20 ppm	96% in 120 min	40.00 emu/g	[151]
Fe_3O_4/$BaTiO_3$	Solvothermal/sol-gel	Degradation of MO and orange II/UV/150 W UV lamp	0.002 g	10 ppm	71.2% in 20 h/MO, 43.7% in 20 h/ orange II	60.50 emu/g	[152]
Fe_3O_4/Cr_2O_3	Wet chemical/ultrasonication	Degradation of 4-CP/UV/12 W low-pressure Hg lamp	0.100 g	1.29 ppm	100% in 150 min	~20 emu/g	[153]
Cu_2O/chitosan/Fe_3O_4	Precipitation-reduction	Degradation of Reactive Brilliant red X-3B (X-3B)/Vis/500 W W-halogen lamp	0.100 g	50 ppm	99.7% in 50 min	15.1 emu/g	[154]
Fe_3O_4/AgBr	Precipitation route	Degradation of MO/Vis/300 W Xe arc lamp/420 nm UV filter	0.100 g	20 ppm	85% in 12 min	No data	[155]
RGO/Ag/AgCl/Fe_3O_4	Solvothermal/deposition-precipitation	Degradation of MB and RhB/Vis/500 W Xe arc/10 cm water filter	0.100 g	10 ppm	97.4% in 100 min/MB, 97.9% in 120 min/RhB	18.8 emu/g	[156]
Metalloporphyrin/Fe_3O_4	Covalent conjugation	Degradation of AO 7/Vis/125 W W-halogen lamp	0.444 g	17.5 ppm	69.0% in 5 h	61.45 emu/g	[157]
Au(Ag)/AgCl/Fe_3O_4@PDA@Au	Solvothermal/galvanic replacement	Degradation of MB/Vis	0.004 g	5 ppm	100% in 20 min	5.40 emu/g	[158]
Fe_3O_4@resorcinol-formaldehyde–Ag	*In situ* polymerisation/reduction	Inactivation of *S. aureus*, *E. coli* and degradation of 4-nitrophenol (4-NP), MB and RhB/Vis/No data on light source	0.010 g	16 ppm/ RhB/MB/4-NP and 10^7 CFU/mL/ bacteria	1.5 < OD in 6 h/ *E. coli*, ~1.0 OD in 6 h, *S. aureus*, ~100% in 3 min/ 4-NP, ~100% in 4 min/MB and ~100% in 3 min/RhB	~30 emu/g	[26]
Poly(p-phenylenediamine)–Fe_3O_4	Chemical oxidation polymerisation	Degradation of bromocresol green (BG), blue (BB), purple (BP), RhB, neutral red (NR), MB, Sudan III (SIII), MO and Congo red (CR)/UV (500 W Hg)/Vis (500 W Xe lamp/420 nm UV filter)	0.025 g	50 ppm	~95% in 1100 min/ BB/UV, ~80% in 1100 min/BB/Vis, ~100% in 1100 min/ BG/UV, ~90% in 1100 min/BG/Vis	No data	[159]

Table 2. *Cont.*

Sample	Preparation Method	Application	Catalyst Dose	Pollutant Concentration	Degradation Efficiency	Magnetisation Saturation	Reference
Polypyrrole (PPY)/ Fe_3O_4/ZnO	*In situ* polymerisation	Degradation of MB/UV/8 W germicidal lamp	0.200 g	10 ppm	85.2% in 4 h	No data	[160]
Fe_3O_4/GO/Ag_3PO_4	Co-precipitation/ ultrasonication	Degradation of MB/Vis/250 W halogen lamp/400 nm UV filter	0.025 g	20 ppm	100% in 10 min	12.56 emu/g	[161]
RGO/Fe_3O_4	*In situ* chemical synthesis	Degradation of MB/natural sunlight/bright sunny days/ 9.00 am to 2.00 pm	0.002 g	10 ppm	100% in 60 min	30.30 emu/g	[162]
ZrO_2/Fe_3O_4/chitosan	Co-precipitation/refluxing	Reduction of Cr(VI) and degradation of 4-CP/ natural sunlight	0.050 g/ Cr(III), 0.010 g/ 4-CP	70 ppm/$K_2Cr_2O_7$, 20 ppm/4-CP	88.6% in 180 min/4-CP, 90.2% in 180 min/Cr(VI)	42.00 emu/g	[115]
Cu_2O/Fe_3O_4	Solvothermal/precipitation	Degradation of MO/Vis/500 W Xe lamp/420 nm UV filter	0.100 g	30 ppm	90% in 90 min	41.70 emu/g	[163]
$FeWO_4$/Fe_3O_4	Hydrothermal	Degradation of MB/UV-Vis/ 500 W Xe lamp	0.020 g	20 ppm	97.1% in 60 min	9.00 emu/g	[164]
Fe_3O_4@carbon quantum dots (CQDs)	Hydrothermal	Degradation of MB/Vis75 W Xe lamp/420 UV filter	0.001 g	1.00 ppm	94.4% in 30 min	33.80 emu/g	[165]
BiOBr@SiO_2@Fe_3O_4	Hydrothermal/ Stobber method	2,2-bis(4-hydroxyphenyl)propane (BPA)/500 W Xe lamp/ 420 UV filter	0.100 g	20 ppm	87.0% in 50 min	No data	[119]

2.4. Ferrites (MFe_2O_4)-based Magnetic Photocatalysts

The spinel ferrites with the chemical formula MFe_2O_4, where M is a cation such as Mg^{2+}, Cu^{2+}, Zn^{2+}, Ni^{2+}, Co^{2+}, *etc.*, are popular materials due to their narrow band gaps, which endow them with remarkable visible light response. Moreover, ferrites show good chemical, thermal, and ferromagnetic properties, numerous oxygen vacancies, and a high density of surface hydroxyl groups [166,167]. In terms of the crystal structure of ferrites, the oxygen atoms form a face-centred cubic (fcc) close packing, while the M^{2+} and Fe^{2+} cations occupy either octahedral or tetrahedral interstitial sites [168]. Generally, ferrites have attracted tremendous interests in various applications such as fabrication of memory devices, biotechnology, catalysts for organic reactions, water splitting, pollution remediation, lithium ion batteries, *etc.* [169–172]. Among the ferrites, zinc ferrite ($ZnFe_2O_4$) is one of the most attractive ferrite due to its photochemical and thermal stability, low toxicity, narrow band gap (1.9 eV), natural abundance, good magnetic properties, and easy preparation [64,173,174]. However, as a pristine photocatalyst, $ZnFe_2O_4$ show low photocatalytic activity (low quantum efficiency) due to the high recombination rate of the photogenerated charge carriers, unconvincing photoelectric conversion, and low valence band potential [64].

In an attempt to improve the photocatalytic performance of $ZnFe_2O_4$, laser ablation obtained $ZnO_x(OH)_x$ and FeO_x colloids were used as precursors to uniformly deposit $ZnFe_2O_4$ nanoparticles on RGO sheets to form a magnetic RGO/$ZnFe_2O_4$ nanocomposite. The RGO/$ZnFe_2O_4$ nanocomposite exhibited improved charge separation and photocatalytic activity towards MB degradation under visible light irradiation [175]. In a similar work by Yang *et al.*, $ZnFe_2O_4$ nanocrystals were confined within an interconnected graphene network, which served as dispersing agents, as transport channels for electrons, and as electron scavengers and reservoirs to minimise recombination. Enhanced visible light photocatalytic degradation of MB was observed over the nanocomposite photocatalyst [176]. In the RGO/$ZnFe_2O_4$ nanocomposite, electrons are excited by visible light from the valence band to the conduction band of $ZnFe_2O_4$, and these electrons quickly transfer to the RGO skeleton where they are trapped by adsorbed oxygen to form superoxide radicals (Figure 6a). The holes are confined to the valence band of $ZnFe_2O_4$ where they directly oxidise the pollutants since they are not positive enough to react with water to form the hydroxyl radicals [175,176]. More interestingly, the RGO/$ZnFe_2O_4$ nanocomposites showed good stability and recyclability and were easily separable using an external magnetic field owing to the good magnetic response (Figure 6b). The presence of RGO ensured that the electrons and holes are located at different parts of the nanocomposite, thereby ensuring efficient charge separation.

Enhanced visible light photocatalytic degradation of 17α-ethinylestradiol (EE 2) was observed over magnetic $ZnFe_2O_4$–Ag/RGO nanocomposite prepared via a hydrothermal method. In terms of degradation kinetics, the nanocomposite photocatalyst showed the highest activity, which was 14.6 and 5.6 times that of $ZnFe_2O_4$ and $ZnFe_2O_4$/RGO, respectively. This could be credited to the combined contribution of RGO, Ag, and $ZnFe_2O_4$ in the nanocomposite, resulting in an improved surface area, efficient charge separation and transportation, minimal aggregation, and improved visible light utilization [177]. Chen and coworkers used a combination of solvothermal and *in situ* precipitation routes to tailor a magnetic RGO/$ZnFe_2O_4$/Ag_3PO_4 nanocomposite and examined its photocatalytic behaviour towards 2,4-DCP under visible light exposure. The ternary nanocomposite exhibited significantly superior activity over pure Ag_3PO_4 [178]. In the $ZnFe_2O_4$–Ag/RGO heterostructure, electrons excited by visible light from the valence band of $ZnFe_2O_4$ to its conduction band transfer to the Ag nanoparticles and, further, to the RGO skeleton where they are captured by adsorbed oxygen to form the radical species (Figure 6c). The holes directly attack the pollutant to form the degradation products [177]. Similarly, in the RGO/$ZnFe_2O_4$/Ag_3PO_4 ternary heterostructure, a heterojunction type of charge transfer mechanism was the most plausible route (Figure 6d). Both $ZnFe_2O_4$ (band gap, 1.92 eV) and Ag_3PO_4 (band gap, 2.42 eV) are excited by visible light, and electrons are promoted to the conduction bands leaving positive holes in the valence bands. The conduction band potential (−0.39 eV) and valence band potential (+1.49 eV) of $ZnFe_2O_4$ are more negative than those of Ag_3PO_4; therefore, electrons transfer to the conduction band of Ag_3PO_4 and RGO, while the holes transfer in

the opposite direction to the valence band of $ZnFe_2O_4$ [178]. This results in efficient charge separation and the formation of the reactive species.

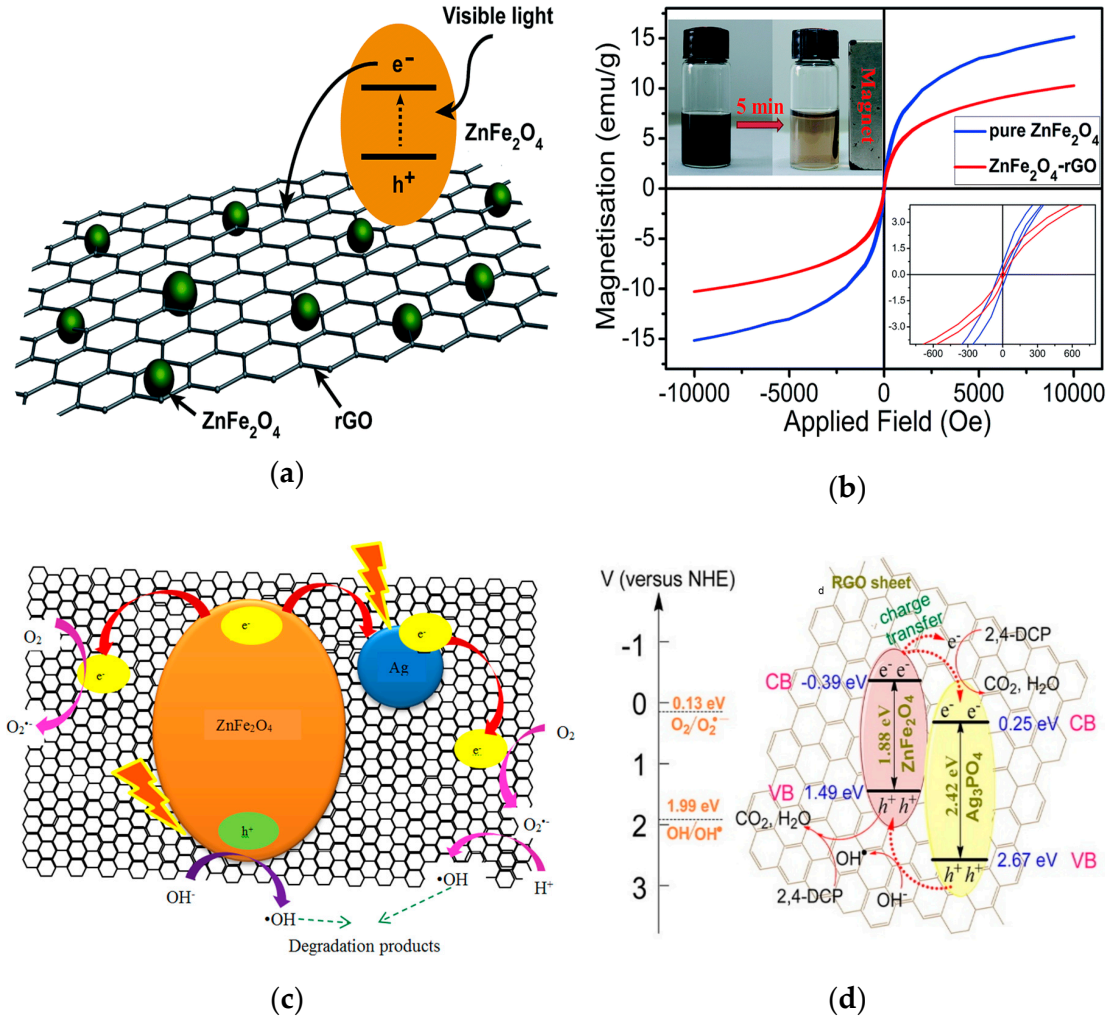

Figure 6. (**a**) Charge transfer route in RGO/$ZnFe_2O_4$; (**b**) magnetisation curves for pure $ZnFe_2O_4$ and RGO/$ZnFe_2O_4$, insert showing magnetic separation of RGO/$ZnFe_2O_4$ (Reproduced with permission from [175], Copyright 2014, RSC); charge transfer mechanism in (**c**) $ZnFe_2O_4$–Ag/RGO (Reproduced with permission from [177], Copyright 2016, Wiley) and (**d**) RGO/$ZnFe_2O_4$/Ag_3PO_4. (Reproduced with permission from [178], Copyright 2016, ACS.

Several other interesting $ZnFe_2O_4$-based magnetic nanocomposite photocatalysts such as $ZnFe_2O_4$/ZnO/Ag_3PO_4 [64], $ZnFe_2O_4$/ZnO [179], N-TiO_2/$ZnFe_2O_4$ [180], $ZnFe_2O_4$/Ag_3PO_4 [38], and Ag/ZnO/$ZnFe_2O_4$ [181] have recently been fabricated, and their photocatalytic properties were examined for the degradation of various pollutants in water. Notably, coupling the various semiconductors with $ZnFe_2O_4$ not only improved the overall visible response and photocatalytic properties of the photocatalysts but also introduced magnetic behaviour, which then allowed for easy separation using an external magnetic field.

Nickel ferrite ($NiFe_2O_4$) is another commonly exploited ferrite with a narrow band gap (1.7 eV), good magnetic properties, and high chemical and thermal stability. Structurally, $NiFe_2O_4$ has a typical inverse spinel structure and is ferromagnetic in nature. Its magnetism stems from the magnetic moment of antiparallel spins between Fe^{3+} cations occupying tetrahedral sites and Ni^{2+} cations sitting at octahedral sites [172,182,183]. Pure $NiFe_2O_4$ exhibits very low photocatalytic activity due to a high recombination rate of the charge carriers and the aggregation of the nanoparticles. However,

$NiFe_2O_4$ is an attractive semiconductor to couple with other semiconductors or carbon nanomaterials and form nanocomposite photocatalysts with improved activity and, most importantly, could easily be separated using a magnet [167,184,185]. For example, magnetically separable AgBr/$NiFe_2O_4$ nanocomposite photocatalyst prepared via a combination of hydrothermal and an ultrasound-assisted precipitation method showed improved photocatalytic performance towards RhB under visible light illumination [186]. Ji and coworkers observed a significant improvement in the photocatalytic activity of magnetic g-C_3N_4/$NiFe_2O_4$ towards MB degradation, reaching 87% in 4 h of visible light irradiation [172]. In another example, magnetic Ag_3PO_4/$NiFe_2O_4$ nanocomposite tailored using an *in situ* precipitation method exhibited better visible light-driven photocatalytic activity towards MB compared to Ag_3PO_4 and $NiFe_3O_4$, individually [184]. $NiFe_2O_4$-based magnetic nanocomposites incorporating carbon nanomaterials such as Pd-$NiFe_2O_4$/RGO [27] and $NiFe_2O_4$/MWCNTs [187] have also shown remarkable enhancement in photocatalytic activity owing to the synergy between the carbon nanomaterials and $NiFe_2O_4$, which resulted in improved optical properties, charge separation, and transportation and specific surface area [27,187].

In all the $NiFe_2O_4$-incorporating photocatalysts, $NiFe_2O_4$ is excited upon the absorption of visible light. The charge transfer process depends on the other semiconductors involved in the nanocomposites. For example in AgBr/$NiFe_2O_4$ and Ag_3PO_4/$NiFe_2O_4$, in addition to $NiFe_2O_4$, AgBr and Ag_3PO_4 are also excited by visible light, and electrons are promoted to their conduction bands, leaving holes in the valence bands. The electrons transfer from the conduction band of $NiFe_2O_4$, since it is more negative, to the conduction bands of AgBr and Ag_3PO_4. Accordingly, the holes transfer from the valence bands of AgBr and Ag_3PO_4 to the valence band of $NiFe_2O_4$ where they are involved in the degradation of the pollutants [184,186]. Meanwhile, in g-C_3N_4/$NiFe_2O_4$ (both semiconductors are visible active), the electrons transfer from the conduction band of g-C_3N_4 to the conduction band of $NiFe_2O_4$, and the holes transfer in the opposite direction to the valence band of g-C_3N_4 (Figure 7a) [172]. Charge separation efficiency is greatly improved upon coupling $NiFe_2O_4$ with the other semiconductors since the holes and electrons are located at different sites in the nanocomposites. Moreover, the presence of $NiFe_2O_4$ nanoparticles in the nanocomposites endowed them with good magnetic response, which allowed for easy magnetic separation.

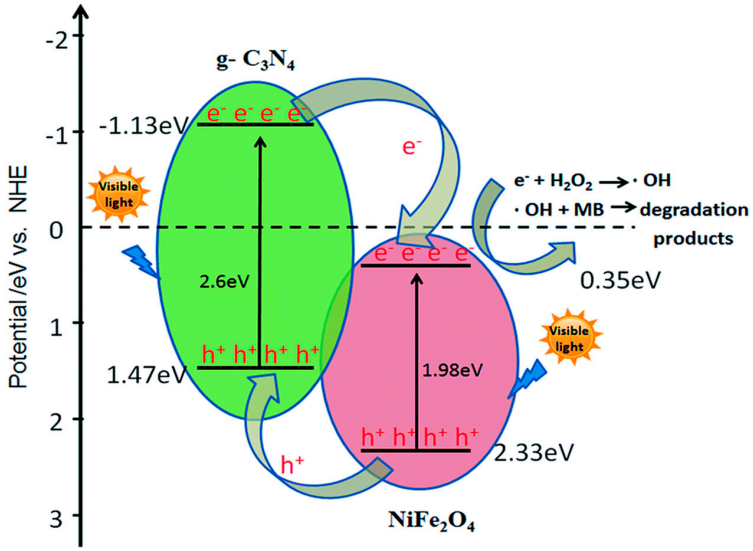

Figure 7. Charge transfer route in g-C_3N_4/$NiFe_2O_4$. Reproduced with permission from [172]. Copyright 2015, RSC.

Cobalt ferrite ($CoFe_2O_4$) is another important magnetic material with several attractive properties such as a crystallisation temperature similar to that of TiO_2, remarkable electromagnetic behaviour, high cubic magnetocrystalline anisotropy, good chemical stability, and high mechanical hardness [188–191].

Coupling $CoFe_2O_4$ with other semiconductors, carbon nanomaterials and conducting polymers are some of the strategies explored in order to benefit from its optical and magnetic properties. Pristine $CoFe_2O_4$ shows poor photocatalytic efficiency due to the high recombination rate of the charge carriers [61,192,193]. Kim *et al.* prepared hollow cobalt ferrite-polyaniline ($CoFe_2O_4$-PANI) nanofibres using the electrospinning method, calcination, and *in situ* chemical oxidative polymerisation, in succession. It was observed that the nanocomposite was magnetically separable and also showed significantly higher visible light photocatalytic degradation of MO, which was 80 times the activity of neat $CoFe_2O_4$ [61]. Hydrothermally prepared magnetic $CoFe_2O_4$/graphene (GR) nanocomposites with varying GR loadings exhibited improved visible light photocatalytic properties towards MB degradation compared to pristine $CoFe_2O_4$. At an optimum GR loading of 10%, the nanocomposite reached 100% MB degradation in 60 min, while the neat $CoFe_2O_4$ could only manage a low 34% degradation in twice the irradiation time [192]. The enhanced activity could be ascribed to the formation of heterojunctions between $CoFe_2O_4$ and GR, which allowed for the efficient separation of the charge carriers. Upon excitation by visible light, the electrons in the conduction band of $CoFe_2O_4$ transfer to GR, where they are trapped by molecular oxygen adsorbed on the surface [192]. A similar scenario was highlighted as responsible for the improved activity of $CoFe_2O_4$-PANI, whereby the electrons are transferred to the conduction band of $CoFe_2O_4$ from PANI while the holes transfer in the opposite direction to PANI [61]. The electrons and holes are kept apart, which ensures their availability to form the active species responsible for pollutant degradation.

Enhanced visible light photocatalytic decomposition of MB was reported over $CoFe_2O_4$ decorated CdS nanorods ($CoFe_2O_4$/CdS, prepared via a soft chemical method. The composite nanorods exhibited better activity than CdS and $CoFe_2O_4$, individually, and were magnetically separable [193]. Three-dimensional (3D) urchin-like TiO_2, prepared hydrothermally, was decorated with $CoFe_2O_4$ using a co-precipitation strategy to yield the nanocomposite photocatalyst $CoFe_2O_4$/TiO_2 with improved photocatalytic properties compared to the individual materials. Upon UV light illumination, the nanocomposite reached 98.9% MB degradation, while 79.9% MB decomposition was realised when the urchin-like TiO_2 was used as the photocatalyst [194]. Moreover, the nanocomposite photocatalyst showed good stability and recyclability, reaching 93.8% MB degradation in the fifth cycles while still maintaining good magnetic properties [194]. Impressive photocatalytic activity and versatility was observed for $CoFe_2O_4$/BiOX (X = Cl, Br and I) nanocomposites towards the UV and visible light photocatalytic decomposition of MO, RhB, MB, and their mixture (MO + MB + RhB) [195]. Similarly, Xu and coworkers examined the photocatalytic properties and versatile nature of the Ag/AgCl/$CoFe_2O_4$ nanocomposite by employing the photocatalyst for the decomposition of MO, bisphenol A (BPA), ciprofloxacin (CIP), and the deactivation of *E. coli*. The nanocomposite photocatalyst displayed outstanding photocatalytic performance towards both coloured (MO) and colourless (BPA and CIP) pollutants as well as microbial pollutants, reaching 93.4% in 150 min for MO and 100% in 90 min for CIP, and almost all of the *E. coli* were deactivated in just 30 min of visible light illumination [196]. In all the $CoFe_2O_4$-incorporating nanocomposites, the enhancement in activity could be ascribed to the formation of a heterojunction between $CoFe_2O_4$ and the other semiconductor, which allowed efficient charge separation and formation of the reactive species responsible for pollutant degradation. In addition, the presence of $CoFe_2O_4$ endowed the nanocomposite photocatalysts with sufficient magnetic sensitivity for easy separation using an external magnetic field [193–196]. Similar results have been reported for other $CoFe_2O_4$-based magnetic photocatalysts such as $CoFe_2O_4$/MCM-41/TiO_2 [197], Fe,N-TiO_2/$CoFe_2O_4$ [198], and BiOBr/$CoFe_2O_4$ [65].

A host of other ferrite-based magnetic nanocomposite photocatalysts (Table 3) have been designed and tailored for the removal of various pollutants in water, for which their photocatalytic properties were also examined. Enhanced photocatalytic performance has been observed upon the incorporation of the ferrites. Moreover, the presence of these ferrites induced magnetic response in the photocatalyst, which aids the separation process for easy recovery and recycling of the photocatalysts. Despite the decrease in magnetisation saturation of the nanocomposites compared to the neat ferrites, the photocatalyst retained enough magnetic response to enable separation using an external magnet.

Table 3. Summary of the photocatalytic properties of ferrite-based photocatalysts.

Sample	Preparation Method	Application	Catalyst Dose	Pollutant Concentration	Degradation Efficiency	Magnetisation Saturation	Reference
P25/$CoFe_2O_4$/RGO	Hydrothermal	Degradation of MB, MO, neutral dark yellow (NDY)/Vis/500 W Xe lamp/420 nmUV filter	0.010 g	40 ppm	~90 mg/g in 60 min/MB, ~20 mg/g in 60 min and 10 mg/g in 60 min	~35 emu/g	[169]
$Mn_xMg_{1-x}Fe_2O_4$ ($0.0 \leqslant x \leqslant 0.5$)	Microwave-assisted combustion	Degradation of 4-CP/Vis/ 8 × 8 W medium pressure Hg lamps	0.030 g	200 ppm	~98% in 300 min	64.67 emu/g	[199]
Ag/TiO_2/$NiFe_2O_4$	Photodeposition/solvothermal	Degradation of MO/Vis/100 W LED	0.100 g	10 ppm	100% in 120 min	No data	[200]
TiO_2@SiO_2@Ni-Cu-$ZnFe_2O_4$	Chemical co-precipitation	Degradation of MB/simulated solar light/35 W Xe arc lamp	0.400 g	10 ppm	83.9% in 6 h	37.45 emu/g	[201]
$CoFe_2O_4$/TiO_2	Co-precipitation	Degradation of Reactive Red 120 (RR 120)/Vis/ 150 W W-halogen lamp	0.400 g	14.70 ppm	4.98×10^{-9} S^{-1}	~0.2 emu/g	[202]
Ag/$NiFe_2O_4$	Combustion	Degradation of MB/Vis/300 W Xe lamp/450 nm UV filter	0.025 g	20 ppm	~80% in 120 min	~20 emu/g	[80]
$NiFe_2O_4$/TiO_2-SiO_2	Modified sol-gel/solvothermal	Degradation of cyanide/Vis/150 W blue fluorescent lamp/420 nm UV filter	No data	100 ppm	100% in 60 min	42.7 emu/g	[203]
$MgFe_2O_4$-ZnO	Solution method/chemical co-precipitation	Degradation of RhB/Vis/500 W Xe lamp/420 nm UV filter	0.050 g	4.40 ppm	100% in 120 min	21.37 emu/g	[204]
PANI-$CoFe_2O_4$-TiO_2	Hydrothermal/*in situ* chemical deposition	Degradation of MB/UV (500 W Xe lamp)/Vis/500 W Xe lamp/400 nm UV filter	0.100 g	50 ppm	0.0962/min/UV and 0.0110/min/Vis	11.4 emu/g	[205]
$Bi_{25}FeO_{40}$-RGO	Hydrothermal	Degradation of MB/Vis/500 W Xe lamp/400 nm UV filter	0.080 g	28.80 ppm	92.8% in 180 min	10.50 emu/g	[206]
BiOCl-$SrFe_{12}O_{19}$	Hydrothermal	Degradation of MB/UV/Vis/No data on light source	0.400 g	10 ppm	99% in 50 min/UV, 67.8% in 8 h/Vis	15.13 emu/g	[207]

Table 3. *Cont.*

Sample	Preparation Method	Application	Catalyst Dose	Pollutant Concentration	Degradation Efficiency	Magnetisation Saturation	Reference
$CuFe_2O_4@C_3N_4$	Self-assembly route	Degradation of orange II/Vis/500 W Xe lamp/420 nm UV filter	0.010 g	9.81 ppm	100% in 90 min	No data	[40]
$Co_{0.6}Zn_{0.4}Mn_xFe_{2-x}O_4$ (x = 0.2–1.0)	Sol-gel auto-combustion	Degradation of MO/Vis/400 W Hg lamp	0.100 g	30 ppm	94% in 60 min	39.51 emu/g	[208]
$Ni_{0.5}Zn_{0.5}Fe_2O_4/Zn_{0.95}Ni_{0.05}$	Egg albumen assisted sol-gel	Degradation of RhB/natural sunlight/sunny days/11 am to 3 pm.	0.010 g	20 ppm	~90% in 4 h	8.00 emu/g	[209]
$CdFe_2O_4$/GR	Hydrothermal	Degradation of MB/Vis/500 W Xe lamp/420 nm UV filter	0.100 g	10 ppm	89.2% in 4 h	14.26 emu/g	[82]
$Mn_xZn_{1-x}Fe_2O_4$-TiO_2 ($0.0 \leqslant x \leqslant 0.5$)	Auto-combustion	Degradation of 4-CP/UV/8 × 8 W low pressure Hg lamps	0.030 g	200 ppm	~98% in 270 min	45.17 emu/g	[210]
$Co_{0.6}Zn_{0.4}Cu_xFe_{2-x}O_4$	Sol-gel auto-combustion	Degradation of MO/Vis/400 W Hg lamp	0.100 g	30 ppm	86% in 60 min	38.02 emu/g	[211]
$Co_xZn_{1-x}Fe_2O_4$-GR	Chemical co-precipitation/ultrasonication	Degradation of MB/Vis/No data on light source	0.100 g	5 ppm	>95% in 60 min	No data	[212]
Sr-$TiO_2/Ni_{0.6}Zn_{0.4}Fe_2O_4$	Combustion/sol-gel	Degradation of BPA/UV (10 W low pressure Hg lamp)/Vis/500 W Xe arc lamp	0.150 g	10 ppm	100% in 4 h/UV, 90% in 4 h/Vis	19.04 emu/g	[213]
$CoFe_2O_4$-GR	Combustion	Degradation of MB/Vis/300 W Xe lamp/450 nm UV filter	0.025 g	20 ppm	100% in 120 min	5.3 emu/g	[166]
$MnFe_2O_4$/g-C_3N_4/TiO_2	Chemical impregnation	Degradation of MO/Simulated solar light/150 W Xe arc lamp	0.050g	10 ppm	99.3% in 180 min	0.065 emu/g	[214]
$Ni_{1-x}Co_xFe_2O_4$	Hydrothermal	Degradation of malachite green (MG)/natural sunlight (200–250 Wm^{-2})	0.025 g	0.365 ppm	~100% in 60 min	~50.7–64.2 emu/g.	[215]
$Mn_xZn_{1-x}Fe_2O_4/\beta$-$Bi_2O_3$	Dip-calcination	Degradation of RhB/Simulated solar light/300 W Xe lamp	0.200g	10 ppm	99.1% in 150 min	7.01 emu/g	[216]

Table 3. *Cont.*

Sample	Preparation Method	Application	Catalyst Dose	Pollutant Concentration	Degradation Efficiency	Magnetisation Saturation	Reference
$Zn_{1-x}Co_xFe_2O_4$	Hydrothermal	Degradation of MB/Natural sunlight	0.050 g	3.20 ppm	~88% in 270 min	~50 emu/g	[217]
$SrFeO_{3-x}$/g-C_3N_4	Sintering method	Degradation of chloramphenicol (CAP) and crystal violet (CV)/Vis/ 150 W Xe arc lamp	0.010 g	10 ppm	91.3% in 96 h/CAP, 99.9% in 12 h/CV	~0.17 emu/g	[41]
$CoFe_2O_4$/GR/CdS	Solvothermal	Degradation of MB/daylight/40 W daylight lamp	0.025 g	20 ppm	80% in 180 min	18.00 emu/g	[218]
ZnO/$CoFe_2O_4$	Co-precipitation	Degradation of direct blue 71 (BD 71)/150 W W-halogen lamp	0.160 g	38.64 ppm	~100% in 30 min	~0.040 emu/g	[219]

3. Summary Remarks and Future Outlook

The development of efficient visible light photocatalytic degradation of pollutants and easy recovery and recyclability of the photocatalyst is an exciting prospect in water treatment. The incorporation of magnetic nanoparticles such as haematite, maghemite, magnetite, and the ferrites into various photocatalyst matrices provides an attractive strategy to enhance the optical properties, charge separation efficiency, and the overall photocatalytic activity. Most interestingly, the presence of the magnetic nanoparticles endow the nanocomposite photocatalyst with sufficient magnetic response to enable separation of the photocatalyst using an external magnetic field. However, careful control of the magnetic nanoparticle, especially loading maghemite and magnetite, is important in ensuring a balance between good magnetic response and the detrimental effect of recombination that occurs on the surface of the nanoparticles. Alternatively, silica is used as a barrier between the magnetic core and the other semiconductor coupled with maghemite or magnetite. This prevents charge transfer between the coupled materials that could otherwise result in photodissolution and recombination. The incorporation of the ferrites in various photocatalysts provides more beneficial properties than just good magnetic response; they contribute towards visible light absorption, charge separation, and the photocatalytic performance of the nanocomposite photocatalyst. Therefore, the ferrites are the most attractive nanoparticles compared to haematite, maghemite, and magnetite, in terms of their photocatalytic performance and multifaceted contribution in the magnetic nanocomposites. However, a systematic, comparative study of the photocatalytic performance of the ferrites, haematite, magnetite, and maghemite is seldom reported, and this makes it difficult to map a way forward in terms of exploiting the best materials for photocatalytic applications.

Despite the promising results regarding visible-light-active magnetic photocatalysts, there are still some challenges that possibly hinder the practical exploitation of these materials. The most obvious problem relates to the reaction kinetics; most of the degradation experiments are slow (may take several hours) despite the improvements in visible light absorption of the photocatalyst, and this presents a massive challenge for practical applications. Secondly, work still needs to be done to develop synthesis routes that will ensure uniform shape and size of the magnetic particles as well as their uniform distribution within the nanocomposite matrix in order to ensure good magnetic response and efficient recovery. Strong contact between the magnetic nanoparticles and the other semiconductor particles is crucial in ensuring minimal leaching out and loss of the photocatalytic activity and magnetic response. In the magnetic core-shell structures, careful control of the thickness of the silica shell is important, as this will affect the magnetic response of the composite material. Extensive theoretical studies are needed in order to understand the interactions between the magnetic nanoparticles and the other semiconductor nanoparticles in the nanocomposites; this can help design and tailor materials with good heterojunctions that promote efficient charge separation. Moreover, theoretical studies can provide a good idea of the optimum loadings of the magnetic nanoparticles in the photocatalyst to ensure good magnetic response and minimal recombination. In most cases, the magnetisation saturation of the magnetic nanoparticles decrease significantly upon coupling with the non-magnetic components of the nanocomposite photocatalyst, which has a negative bearing on the separation efficiency and recovery of the photocatalyst. Work still needs to be done to ensure that nanocomposites retain sufficiently high magnetic response in order to enable efficient magnetic separation.

Acknowledgments: Financial support from the College of Science, Engineering and Technology (CSET) of the University of South Africa is highly appreciated.

Author Contributions: Gcina Mamba conceived the idea of writing a review on magnetically separable photocatalysts and wrote the introduction and Sections 2.1–2.3. Ajay Mishra is the project leader and was responsible for structuring the review, writing Section 2.4, and editing the entire review article.

Conflicts of Interest: The authors declare no conflict of interest.

References

1. Fersi, C.; Gzara, L.; Dhahbi, M. Treatment of textile effluents by membrane technologies. *Desalination* **2005**, *185*, 399–409. [CrossRef]
2. Pendergast, M.M.; Hoek, E.M.V. A review of water treatment membrane nanotechnologies. *Energy Environ. Sci.* **2011**, *4*, 1946–1971. [CrossRef]
3. Wang, H.; Zheng, X.W.; Su, J.Q.; Tian, Y.; Xiong, X.J.; Zheng, T.L. Biological decolorization of the reactive dyes Reactive Black 5 by a novel isolated bacterial strain *Enterobacter* sp. EC3. *J. Hazard. Mater.* **2009**, *171*, 654–659. [CrossRef] [PubMed]
4. Kumari, K.; Abraham, T.E. Biosorption of anionic textile dyes by nonviable biomass of fungi and yeast. *Bioresour. Technol.* **2007**, *98*, 1704–1710. [CrossRef] [PubMed]
5. Soutsas, K.; Karayannis, V.; Poulios, I.; Riga, A.; Ntampegliotis, K.; Spiliotis, X.; Papapolymerou, G. Decolorization and degradation of reactive azo dyes via heterogeneous photocatalytic processes. *Desalination* **2010**, *250*, 345–350. [CrossRef]
6. Wu, J.; Doan, H.; Upreti, S. Decolorization of aqueous textile reactive dye by ozone. *Chem. Eng. J.* **2008**, *142*, 156–160. [CrossRef]
7. Harsha, N.; Krishna, K.V.S.; Renuka, N.K.; Shukla, S. Facile synthesis of g–Fe_2O_3 nanoparticles integrated $H_2Ti_3O_7$ nanotubes structure as a magnetically recyclable dye-removal catalyst. *RSC Adv.* **2015**, *5*, 30354–30362. [CrossRef]
8. Li, K.; Chai, F.; Zhao, Y.; Guo, X. Facile synthesis of magnetic Fe_3O_4/$CeCO_3OH$ composites with excellent adsorption capability for small cationic dyes. *RSC Adv.* **2015**, *5*, 94397–94404. [CrossRef]
9. Song, S.; Fan, J.; He, Z.; Zhan, L.; Liu, Z.; Chen, J.; Xu, X. Electrochemical degradation of azo dye C.I. Reactive Red 195 by anodic oxidation on Ti/SnO_2-Sb/PbO_2 electrodes. *Electrochim. Acta* **2010**, *55*, 3606–3613. [CrossRef]
10. Faouzi, A.M.; Nasr, B.; Abdellatif, G. Electrochemical degradation of anthraquinone dye Alizarin Red S by anodic oxidation on boron-doped diamond. *Dyes Pigments* **2007**, *73*, 86–89. [CrossRef]
11. Rodrigues, C.S.D.; Madeira, L.M.; Boaventura, R.A.R. Synthetic textile dyeing wastewater treatment by integration of advanced oxidation and biological processes—Performance analysis with costs reduction. *J. Environ. Chem. Eng.* **2014**, *2*, 1027–1039. [CrossRef]
12. Basha, C.A.; Selvakumar, K.V.; Prabhu, H.J.; Sivashanmugam, P.; Lee, C.W. Degradation studies for textile reactive dye by combined electrochemical, microbial and photocatalytic methods. *Sep. Purif. Technol.* **2011**, *79*, 303–309. [CrossRef]
13. Berberidou, C.; Avlonitis, S.; Poulios, I. Dyestuff effluent treatment by integrated sequential photocatalytic oxidation and membrane filtration. *Desalination* **2009**, *249*, 1099–1106. [CrossRef]
14. Khouni, I.; Marrot, B.; Moulin, P.; Ben, R. Decolourization of the reconstituted textile effluent by different process treatments: Enzymatic catalysis, coagulation/flocculation and nanofiltration processes. *Desalination* **2011**, *268*, 27–37. [CrossRef]
15. Trzcinski, A.P.; Stuckey, D.C. Inorganic fouling of an anaerobic membrane bioreactor treating leachate from the organic fraction of municipal solid waste (OFMSW) and a polishing aerobic membrane bioreactor. *Bioresour. Technol.* **2016**, *204*, 17–25. [CrossRef] [PubMed]
16. Schulz, M.; Soltani, A.; Zheng, X.; Ernst, M. Effect of inorganic colloidal water constituents on combined low-pressure membrane fouling with natural organic matter (NOM). *J. Membr. Sci.* **2016**, *507*, 154–164. [CrossRef]
17. Hegab, H.M.; Elmekawy, A.; Barclay, T.G.; Michelmore, A.; Zou, L.; Saint, C.P.; Ginic-Markovic, M. Effective in-situ chemical surface modification of forward osmosis membranes with polydopamine-induced graphene oxide for biofouling mitigation. *Desalination* **2016**, *385*, 126–137. [CrossRef]
18. Gottlieb, A.; Shaw, C.; Smith, A.; Wheatley, A.; Forsythe, S. The toxicity of textile reactive azo dyes after hydrolysis and decolourisation. *J. Biotechnol.* **2003**, *101*, 49–56. [CrossRef]
19. Kariyajjanavar, P.; Jogttappa, N.; Nayaka, Y.A. Studies on degradation of reactive textile dyes solution by electrochemical method. *J. Hazard. Mater.* **2011**, *190*, 952–961. [CrossRef] [PubMed]
20. Faouzi Elahmadi, M.; Bensalah, N.; Gadri, A. Treatment of aqueous wastes contaminated with Congo Red dye by electrochemical oxidation and ozonation processes. *J. Hazard. Mater.* **2009**, *168*, 1163–1169. [CrossRef] [PubMed]

21. Mohammad, N.; Arami, M. Degradation and toxicity reduction of textile wastewater using immobilized titania nanophotocatalysis. *J. Photochem. Photobiol. B* **2009**, *94*, 20–24.
22. Aksu, Z.; Dönmez, G. Combined effects of molasses sucrose and reactive dye on the growth and dye bioaccumulation properties of *Candida tropicalis*. *Process Biochem.* **2005**, *40*, 2443–2454. [CrossRef]
23. Yu, W.; Xu, D.; Peng, T. Enhanced photocatalytic activity of g-C_3N_4 for selective CO_2 reduction to CH_3OH via facile coupling of ZnO: A direct Z-scheme mechanism. *J. Mater. Chem. A* **2015**, *3*, 19936–19947. [CrossRef]
24. Lu, D.; Zhang, G.; Wan, Z. Visible-light-driven g-C_3N_4/Ti^{3+}-TiO_2 photocatalyst co-exposed {001} and {101} facets and its enhanced photocatalytic activities for organic pollutant degradation and Cr(VI) reduction. *Appl. Surf. Sci.* **2015**, *358*, 223–230. [CrossRef]
25. Li, G.; Nie, X.; Chen, J.; Jiang, Q.; An, T.; Wong, P.K.; Zhang, H.; Zhao, H.; Yamashita, H. Enhanced visible-light-driven photocatalytic inactivation of *Escherichia coli* using g-C_3N_4/TiO_2 hybrid photocatalyst synthesized using a hydrothermal-calcination approach. *Water Res.* **2015**, *86*, 17–24. [CrossRef] [PubMed]
26. Zhong, Y.; Ni, Y.; Li, S.; Wang, M. Chain-like Fe_3O_4@resorcinol-formaldehyde resins-Ag composite microstructures: Facile construction and applications in antibacterial and catalytic fields. *RSC Adv.* **2016**, *6*, 15831–15837. [CrossRef]
27. Li, Y.; Zhang, Z.; Pei, L.; Li, X.; Fan, T.; Ji, J.; Shen, J.; Ye, M. Multifunctional photocatalytic performances of recyclable Pd-$NiFe_2O_4$/reduced graphene oxide nanocomposites via different co-catalyst strategy. *Appl. Catal. B Environ.* **2016**, *190*, 1–11. [CrossRef]
28. Zeng, B.; Zhang, L.; Wan, X.; Song, H.; Lv, Y. Fabrication of α-Fe_2O_3/g-C_3N_4 composites for cataluminescence sensing of H_2S. *Sens. Actuators Chem.* **2015**, *211*, 370–376. [CrossRef]
29. Wang, G.; Kuang, S.; Zhang, J.; Hou, S.; Nian, S. Graphitic carbon nitride/multiwalled carbon nanotubes composite as Pt-free counter electrode for high-efficiency dye-sensitized solar cells. *Electrochim. Acta* **2016**, *187*, 243–248. [CrossRef]
30. Wang, M.; Yang, X.; Bi, W. Application of magnetic graphitic carbon nitride nanocomposites for the solid-phase extraction of phthalate esters in water samples. *J. Sep. Sci.* **2015**, *38*, 445–452. [CrossRef] [PubMed]
31. Baig, R.B.N.; Verma, S.; Varma, R.S.; Nadagouda, M.N. Magnetic Fe@g-C_3N_4: A photoactive catalyst for the hydrogenation of alkenes and alkynes. *ACS Sustain. Chem. Eng.* **2016**, *4*, 1661–1664. [CrossRef]
32. Preethi, V.; Kanmani, S. Photocatalytic hydrogen production using Fe_2O_3-based core shell nano particles with ZnS and CdS. *Int. J. Hydrogen Energy* **2014**, *39*, 1613–1622. [CrossRef]
33. Cao, M.; Wang, P.; Ao, Y.; Wang, C.; Hou, J.; Qian, J. Visible light activated photocatalytic degradation of tetracycline by a magnetically separable composite photocatalyst: Graphene oxide/magnetite/cerium-doped titania. *J. Colloid Interface Sci.* **2016**, *467*, 129–139. [CrossRef] [PubMed]
34. Bao, X.; Qiang, Z.; Chang, J.; Ben, W.; Qu, J. Synthesis of carbon-coated magnetic nanocomposite (Fe_3O_4@C) and its application for sulfonamide antibiotics removal from water. *J. Environ. Sci.* **2014**, *26*, 962–969. [CrossRef]
35. Zhou, L.; Deng, J.; Zhao, Y.; Liu, W.; An, L.; Chen, F. Preparation and characterization of N–I co-doped nanocrystal anatase TiO_2 with enhanced photocatalytic activity under visible-light irradiation. *Mater. Chem. Phys.* **2009**, *117*, 522–527. [CrossRef]
36. Nolan, N.T.; Synnott, D.W.; Seery, M.K.; Hinder, S.J.; van Wassenhoven, A.; Pillai, S.C. Effect of N-doping on the photocatalytic activity of sol-gel TiO_2. *J. Hazard. Mater.* **2012**, *211–212*, 88–94. [CrossRef] [PubMed]
37. Pany, S.; Parida, K.M. A facile *in situ* approach to fabricate N,S-TiO_2/g-C_3N_4 nanocomposite with excellent activity for visible light induced water splitting for hydrogen evolution. *Phys. Chem. Chem. Phys.* **2015**, *17*, 8070–8077. [CrossRef] [PubMed]
38. Ge, M.; Chen, Y.; Liu, M.; Li, M. Synthesis of magnetically separable Ag_3PO_4/$ZnFe_2O_4$ composite photocatalysts for dye degradation under visible LED light irradiation. *J. Environ. Chem. Eng.* **2015**, *3*, 2809–2815. [CrossRef]
39. Xu, Y.; Huang, S.; Xie, M.; Li, Y.; Jing, L.; Xu, H. Core-shell magnetic Ag/AgCl@Fe_2O_3 photocatalysts with enhanced photoactivity for eliminating bisphenol A and microbial contamination. *New J. Chem.* **2016**, *40*, 3413–3422. [CrossRef]
40. Yao, Y.; Lu, F.; Zhu, Y.; Wei, F.; Liu, X.; Lian, C.; Wang, S. Magnetic core-shell $CuFe_2O_4$@C_3N_4 hybrids for visible light photocatalysis of Orange II. *J. Hazard. Mater.* **2015**, *297*, 224–233. [CrossRef] [PubMed]

41. Lin, H.-P.; Chen, C.-C.; Lee, W.W.; Lai, Y.-Y.; Chen, J.; Chen, Y.; Fu, J.-Y. Synthesis of a $SrFeO_{3-x}$/g-C_3N_4 heterojunction with improved visible-light photocatalytic activities in chloramphenicol and crystal violet degradation. *RSC Adv.* **2015**, *6*, 2323–2336. [CrossRef]
42. Li, G.; Nie, X.; Gao, Y.; An, T. Can environmental pharmaceuticals be photocatalytically degraded and completely mineralized in water using g-C_3N_4/TiO_2 under visible light irradiation?—Implications of persistent toxic intermediates. *Appl. Catal. B Environ.* **2016**, *180*, 726–732. [CrossRef]
43. Zhang, J.; Hu, S.; Wang, Y. A convenient method to prepare a novel alkali metal sodium doped carbon nitride photocatalyst with a tunable band structure. *RSC Adv.* **2014**, *4*, 62912–62919. [CrossRef]
44. Jin, R.; Hu, S.; Gui, J.; Liu, D. A convenient method to prepare novel rare earth metal Ce-doped carbon nitride with enhanced photocatalytic activity under visible light. *Bull. Korean Chem. Soc.* **2015**, *36*, 17–23. [CrossRef]
45. Akpan, U.G.; Hameed, B.H. Enhancement of the photocatalytic activity of TiO_2 by doping it with calcium ions. *J. Colloid Interface Sci.* **2011**, *357*, 168–178. [CrossRef] [PubMed]
46. Inturi, S.N.R.; Boningari, T.; Suidan, M.; Smirniotis, P.G. Visible-light-induced photodegradation of gas phase acetonitrile using aerosol-made transition metal (V, Cr, Fe, Co, Mn, Mo, Ni, Cu, Y, Ce, and Zr) doped TiO_2. *Appl. Catal. B Environ.* **2014**, *144*, 333–342. [CrossRef]
47. Li, Z.; Wang, J.; Zhu, K.; Ma, F.; Meng, A. Ag/g-C_3N_4 composite nanosheets: Synthesis and enhanced visible photocatalytic activities. *Mater. Lett.* **2015**, *145*, 167–170. [CrossRef]
48. Hu, S.; Ma, L.; You, J.; Li, F.; Fan, Z.; Wang, F.; Liu, D.; Gui, J. A simple and efficient method to prepare a phosphorus modified g-C_3N_4 visible light photocatalyst. *RSC Adv.* **2014**, *4*, 21657–21663. [CrossRef]
49. Sun, H.; Wang, S.; Ang, H.M.; Tadé, M.O.; Li, Q. Halogen element modified titanium dioxide for visible light photocatalysis. *Chem. Eng. J.* **2010**, *162*, 437–447. [CrossRef]
50. Dong, G.; Ai, Z.; Zhang, L. Efficient anoxic pollutant removal with oxygen functionalized graphitic carbon nitride under visible light. *RSC Adv.* **2014**, *4*, 5553–5560. [CrossRef]
51. Sharotri, N.; Sud, D. Ultrasound-assisted synthesis and characterization of visible light responsive nitrogen-doped TiO_2 nanomaterials for removal of 2-Chlorophenol. *Desalin. Water Treat.* **2016**, *57*, 8776–8788. [CrossRef]
52. Reszczyńska, J.; Grzyb, T.; Sobczak, J.W.; Lisowski, W.; Gazda, M.; Ohtani, B.; Zaleska, A. Visible light activity of rare earth metal doped (Er^{3+}, Yb^{3+} or Er^{3+}/Yb^{3+}) titania photocatalysts. *Appl. Catal. B: Environ.* **2015**, *163*, 40–49. [CrossRef]
53. Kaur, N.; Kaur, S.; Singh, V. Preparation, characterization and photocatalytic degradation kinetics of Reactive Red dye 198 using N, Fe codoped TiO_2 nanoparticles under visible light. *Desalination Water Treat.* **2016**, *57*, 9237–9246. [CrossRef]
54. Xu, X.; Zhou, X.; Zhang, L.; Xu, L.; Ma, L.; Luo, J.; Li, M.; Zeng, L. Photoredox degradation of different water pollutants (MO, RhB, MB, and Cr(VI)) using Fe-N-S-tri-doped TiO_2 nanophotocatalyst prepared by novel chemical method. *Mater. Res. Bull.* **2015**, *70*, 106–113. [CrossRef]
55. Antonopoulou, M.; Vlastos, D.; Konstantinou, I. Photocatalytic degradation of pentachlorophenol by N-F-TiO_2: Identification of intermediates, mechanism involved, genotoxicity and ecotoxicity evaluation. *Photochem. Photobiol. Sci.* **2015**, *14*, 520–527. [CrossRef] [PubMed]
56. Mamba, G.; Mbianda, X.Y.; Mishra, A.K. Photocatalytic degradation of the diazo dye naphthol blue black in water using MWCNT/Gd,N,S-TiO_2 nanocomposites under simulated solar light. *J. Environ. Sci.* **2015**, *33*, 219–228. [CrossRef] [PubMed]
57. Mamba, G.; Mamo, M.A.; Mbianda, X.Y.; Mishra, A.K. Nd,N,S-TiO_2 decorated on reduced graphene oxide for a visible light active photocatalyst for dye degradation: Comparison to its MWCNT/Nd,N,S-TiO_2 analogue. *Ind. Eng. Chem. Res.* **2014**, *53*, 14329–14338. [CrossRef]
58. Mamba, G.; Mbianda, X.Y.; Mishra, A.K. Enhanced visible light photocatalytic degradation of eriochrome black T and eosin blue shade in water using tridoped titania decorated on SWCNTs and MWCNTs: Effect of the type of carbon nanotube incorporated. *Mater. Chem. Phys.* **2015**, *149–150*, 734–742. [CrossRef]
59. Apostolopoulou, V.; Vakros, J.; Kordulis, C.; Lycourghiotis, A. Preparation and characterization of [60] fullerene nanoparticles supported on titania used as a photocatalyst. *Colloids Surf. A Physicochem. Eng. Asp.* **2009**, *349*, 189–194. [CrossRef]
60. Shang, J.; Zhao, F.; Zhu, T.; Li, J. Photocatalytic degradation of rhodamine B by dye-sensitized TiO_2 under visible-light irradiation. *Sci. China Chem.* **2011**, *54*, 167–172. [CrossRef]

61. Nam, K.; Jung, H.; Lee, W. Hollow cobalt ferrite-polyaniline nanofibers as magnetically separable visible-light photocatalyst for photodegradation of methyl orange. *J. Photochem. Photobiol. A Chem.* **2016**, *321*, 257–265.
62. Kim, G.; Choi, W. Charge-transfer surface complex of EDTA-TiO_2 and its effect on photocatalysis under visible light. *Appl. Catal. B Environ.* **2010**, *100*, 77–83. [CrossRef]
63. Shi, W.; Lu, D.; Wang, L.; Teng, F.; Zhang, J. Core-shell structured Fe_3O_4@SiO_2@CdS nanoparticles with enhanced visible-light photocatalytic photocatalytic activities. *RSC Adv.* **2015**, *5*, 106038–106043. [CrossRef]
64. Li, J.; Liu, Z.; Zhu, Z. Enhanced photocatalytic activity in $ZnFe_2O_4$-ZnO-Ag_3PO_4 hollow nanospheres through the cascadal electron transfer with magnetical separation. *J. Alloys Compd.* **2015**, *636*, 229–233. [CrossRef]
65. Jiang, R.; Zhu, H.; Li, J.; Fu, F.; Yao, J.; Jiang, S.; Zeng, G.-M. Fabrication of novel magnetically separable BiOBr/$CoFe_2O_4$ microspheres and its application in the efficient removal of dye from aqueous phase by an environment-friendly and economical approach. *Appl. Surf. Sci.* **2016**, *364*, 604–612. [CrossRef]
66. Mi, J.; Hwan, Y.; Keun, B.; Ho, S.; Soo, B.; Bin, J. Novel immobilization of titanium dioxide (TiO_2) on the fluidizing carrier and its application to the degradation of azo-dye. *J. Hazard. Mater.* **2006**, *134*, 230–236.
67. Fernhndez, A.; Lassaletta, G.; Jimknez, V.M.; Justo, A. Preparation and characterization of TiO_2 photocatalysts supported on various rigid supports (glass, quartz and stainless steel). Comparative studies of photocatalytic activity in water purification. *Appl. Catal. B Environ.* **1995**, *7*, 49–63. [CrossRef]
68. Carlson, P.J.; Pretzer, L.A.; Boyd, J.E. Solvent deposition of titanium dioxide on acrylic for photocatalytic application. *Ind. Eng. Chem. Res.* **2007**, *46*, 7970–7976. [CrossRef]
69. Arabatzis, I.M.; Antonaraki, S.; Stergiopoulos, T.; Hiskia, A. Preparation, characterization and photocatalytic activity of nanocrystalline thin film TiO_2 catalysts towards 3,5-dichlorophenol degradation. *J. Photochem. Photobiol. A Chem.* **2002**, *149*, 237–245. [CrossRef]
70. Anpo, M.; Zhang, S.G.; Mishima, H.; Matsuoka, M.; Yamashita, H. Design of photocatalysts encapsulated within the zeolite framework and cavities for the decomposition of NO into N_2 and O_2 at normal temperature. *Catal. Today* **1997**, *39*, 159–168. [CrossRef]
71. Rao, N.N.; Chaturvedi, V. Photoactivity of TiO_2-coated pebbles. *Ind. Eng. Chem. Res.* **2007**, *46*, 4406–4414. [CrossRef]
72. Gad-allah, T.A.; Kato, S.; Satokawa, S.; Kojima, T. Treatment of synthetic dyes wastewater utilizing a magnetically separable photocatalyst (TiO_2/SiO_2/Fe_3O_4): Parametric and kinetic studies. *Desalination* **2009**, *244*, 1–11. [CrossRef]
73. Wang, W.; Yao, J. Synthesis of magnetically separable Sn doped magnetite/silica core-shell structure and photocatalytic property. *Mater. Res. Bull.* **2010**, *45*, 710–716. [CrossRef]
74. Belessi, V.; Lambropoulou, D.; Konstantinou, I.; Zboril, R.; Tucek, J.; Jancik, D. Structure and photocatalytic performance of magnetically separable titania photocatalysts for the degradation of propachlor. *Appl. Catal. B Environ.* **2009**, *87*, 181–189. [CrossRef]
75. Linley, S.; Leshuk, T.; Gu, F.X. Synthesis of magnetic rattle-type nanostructures for use in water treatment. *ACS Appl. Mater. Interfaces* **2013**, *5*, 2540–2548. [CrossRef] [PubMed]
76. Kumar, S.; Kumar, B.; Baruah, A.; Shanker, V. Synthesis of magnetically separable and recyclable g-C_3N_4–Fe_3O_4 hybrid nanocomposites with enhanced photocatalytic performance under visible-light irradiation. *J. Phys. Chem. C* **2013**, *117*, 26135–26143. [CrossRef]
77. Yang, J.; Chen, H.; Gao, J.; Yan, T.; Zhou, F.; Cui, S.; Bi, W. Synthesis of Fe_3O_4/g-C_3N_4 nanocomposites and their application in the photodegradation of 2,4,6-trichlorophenol under visible light. *Mater. Lett.* **2016**, *164*, 183–189. [CrossRef]
78. Shih, Y.; Su, C.; Chen, C.; Dong, C. Synthesis of magnetically recoverable ferrite (MFe_2O_4, M = Co, Ni and Fe)-supported TiO_2 photocatalysts for decolorization of methylene blue. *Catal. Commun.* **2015**, *72*, 127–132. [CrossRef]
79. Pang, Y.L.; Lim, S.; Ong, H.C.; Chong, W.T. Synthesis, characteristics and sonocatalytic activities of calcined α-Fe_2O_3 and TiO_2 nanotubes/α-Fe_2O_3 magnetic catalysts in the degradation of Orange G. *Ultrason. Sonochem.* **2016**, *29*, 317–327.
80. Zhang, D.; Pu, X.; Du, K.; Moon, Y.; Jeong, J.; Cai, P.; Kim, S., II; Seo, H.J. Combustion synthesis of magnetic Ag/$NiFe_2O_4$ composites with enhanced visible-light photocatalytic properties. *Sep. Purif. Technol.* **2014**, *137*, 82–85. [CrossRef]

81. Zhao, H.; Zhang, L.; Gu, X.; Li, S.; Li, B.; Wang, H. Fe_2O_3-AgBr nonwoven cloth with hierarchical nanostructures as efficient and easily recyclable macroscale photocatalysts. *RSC Adv.* **2015**, *5*, 10951–10959. [CrossRef]
82. Zhang, D.; Wang, Q.; Wang, L.; Zhang, L. Magnetically separable $CdFe_2O_4$/graphene catalyst and its enhanced photocatalytic properties. *J. Mater. Chem. A* **2015**, *3*, 3576–3585. [CrossRef]
83. Liu, J.; Qiao, S.Z.; Hu, Q.H.; Qing, G.; Lu, M. Magnetic nanocomposites with mesoporous structures: Synthesis and applications. *Small* **2011**, *7*, 425–443. [CrossRef] [PubMed]
84. Polshettiwar, V.; Luque, R.; Fihri, A.; Zhu, H.; Bouhrara, M.; Basset, J. Magnetically recoverable nanocatalysts. *Chem. Rev.* **2011**, *111*, 3036–3075. [CrossRef] [PubMed]
85. Zhang, D.; Zhou, C.; Sun, Z.; Wu, L.-Z.; Tung, C.-H.; Zhang, T. Magnetically recyclable nanocatalysts (MRNCs): A versatile integration of high catalytic activity and facile recovery. *Nanoscale* **2012**, *4*, 6244–6255. [CrossRef] [PubMed]
86. Wang, D.; Astruc, D. Fast-growing field of magnetically recyclable nanocatalysts. *Chem. Rev.* **2014**, *114*, 6949–6985. [CrossRef] [PubMed]
87. Linley, S.; Leshuk, T.; Gu, F.X. Magnetically separable water treatment technologies and their role in future advanced water treatment: A patent review. *CLEAN Soil Air Water* **2013**, *41*, 1152–1156. [CrossRef]
88. Yao, H.; Fan, M.; Wang, Y. Magnetic titanium dioxide based nanomaterials: Synthesis, characteristics, and photocatalytic application in pollutant degradation. *J. Mater. Chem. A* **2015**, *3*, 17511–17524. [CrossRef]
89. Liu, D.; Li, Z.; Wang, W.; Wang, G.; Liu, D. Hematite doped magnetic TiO_2 nanocomposites with improved photocatalytic activity. *J. Alloy Compd.* **2016**, *654*, 491–497. [CrossRef]
90. Shi, Y.; Li, H.; Wang, L.; Shen, W.; Chen, H. Novel α-Fe_2O_3/CdS cornlike nanorods with enhanced photocatalytic performance. *ACS Appl. Mater. Interfaces* **2012**, *4*, 4800–4806. [CrossRef] [PubMed]
91. Xu, Y.; Jing, L.; Chen, X.; Ji, H.; Xu, H.; Li, H. Novel visible-light-driven Fe_2O_3/Ag_3VO_4 composite with enhanced photocatalytic activity toward organic pollutants degradation. *RSC Adv.* **2016**, *6*, 3600–3607. [CrossRef]
92. Xu, Y.; Huang, S.; Xie, M.; Li, Y.; Xu, H.; Huang, L.; Zhang, Q.; Li, H. Magnetically separable Fe_2O_3/g-C_3N_4 catalyst with enhanced photocatalytic activity. *RSC Adv.* **2015**, *5*, 95727–95735. [CrossRef]
93. Kumar, S.V.; Huang, N.M.; Yusoff, N.; Lim, H.N. High performance magnetically separable graphene/zinc oxide nanocomposite. *Mater. Lett.* **2013**, *93*, 411–414. [CrossRef]
94. Wang, H.; Fei, X.; Wang, L.; Li, Y.; Xu, S. Magnetically separable iron oxide nanostructures-TiO_2 nanofibers hierarchical heterostructures: Controlled fabrication and photocatalytic activity. *New J. Chem.* **2011**, *35*, 1795–1802. [CrossRef]
95. Muthukrishnaraj, A.; Vadivel, S.; Kamalakannan, V.P.; Balasubramanian, N. α-Fe_2O_3/reduced graphene oxide nanorod as efficient photocatalyst for methylene blue degradation. *Mater. Res. Innov.* **2016**, *19*, 258–264. [CrossRef]
96. Wu, W.; Zhang, S.; Xiao, X.; Zhou, J.; Ren, F.; Sun, L.; Jiang, C. Controllable synthesis, magnetic properties, and enhanced photocatalytic activity of spindle-like mesoporous α-Fe_2O_3/ZnO core-shell heterostructures. *ACS Appl. Mater. Interfaces* **2012**, *4*, 3602–3609. [CrossRef] [PubMed]
97. Xue, J.; Ma, S.; Zhou, Y.; Zhang, Z.; Liu, X. Fabrication of porous g-C_3N_4/Ag/Fe_2O_3 composites with enhanced visible light photocatalysis performance. *RSC Adv.* **2015**, *5*, 58738–58745. [CrossRef]
98. Liu, X.; Jin, A.; Jia, Y.; Jiang, J.; Hu, N.; Chen, X. Facile synthesis and enhanced visible-light photocatalytic activity of graphitic carbon nitride decorated with ultrafine Fe_2O_3 nanoparticles. *RSC Adv.* **2015**, *5*, 92033–92041. [CrossRef]
99. Theerthagiri, J.; Senthil, R.A.; Priya, A.; Madhavan, J.; Michael, R.J.V.; Ashokkumar, M. Photocatalytic and photoelectrochemical studies of visible-light-active α-Fe_2O_3-g-C_3N_4 nanocomposites. *RSC Adv.* **2014**, *4*, 38222–38229. [CrossRef]
100. Liu, Y.; Yu, Y.X.; Zhang, W. Photoelectrochemical study on charge transfer properties of nanostructured Fe_2O_3 modified by g-C_3N_4. *Int. J. Hydrogen Energy* **2014**, *39*, 9105–9113. [CrossRef]
101. Peng, L.; Xie, T.; Lu, Y.; Fan, H.; Wang, D. Synthesis, photoelectric properties and photocatalytic activity of the Fe_2O_3/TiO_2 heterogeneous photocatalysts. *Phys. Chem. Chem. Phys.* **2010**, *12*, 8033–8041. [CrossRef] [PubMed]

102. Pawar, R.C.; Pyo, Y.; Ahn, S.H.; Lee, C.S. Photoelectrochemical properties and photodegradation of organic pollutants using hematite hybrids modified by gold nanoparticles and graphitic carbon nitride. *Appl. Catal. B Environ.* **2015**, *176–177*, 654–666. [CrossRef]
103. Yamauraa, M.; Camilo, R.L.; Sampaio, L.C.; Macedo, M.A.; Nakamurad, M.; Toma, H.E. Preparation and characterization of (3-aminopropyl) triethoxysilane-coated magnetite nanoparticles. *J. Magn. Magn. Mater.* **2004**, *279*, 210–217. [CrossRef]
104. Tian, B.; Wang, T.; Dong, R.; Bao, S.; Yang, F.; Zhang, J. Core-shell structured–Fe_2O_3@SiO_2@AgBr: Ag composite with high magnetic separation efficiency and excellent visible light activity for acid orange 7 degradation. *Appl. Catal. B Environ.* **2014**, *147*, 22–28. [CrossRef]
105. Idris, A.; Hassan, N.; Rashid, R.; Ngomsik, A. Kinetic and regeneration studies of photocatalytic magnetic separable beads for chromium (VI) reduction under sunlight. *J. Hazard. Mater.* **2011**, *186*, 629–635. [CrossRef] [PubMed]
106. Yu, X.; Liu, S.; Yu, J. Superparamagnetic γ-Fe_2O_3@SiO_2@TiO_2 composite microspheres with superior photocatalytic properties. *Appl. Catal. B Environ.* **2011**, *104*, 12–20. [CrossRef]
107. Lin, Y.; Chang, C. Magnetic mesoporous iron oxide/carbon aerogel photocatalysts with adsorption ability for organic dye removal. *RSC Adv.* **2014**, *4*, 28628–28631. [CrossRef]
108. Zhang, Y.; Zhang, Y.; Tan, J. Novel magnetically separable AgCl/iron oxide composites with enhanced photocatalytic activity driven by visible light. *J. Alloy. Compd.* **2013**, *574*, 383–390. [CrossRef]
109. Ye, S.; Qiu, L.-G.; Yuan, Y.-P.; Zhu, Y.-J.; Xia, J.; Zhu, J.-F. Facile fabrication of magnetically separable graphitic carbon nitride photocatalysts with enhanced photocatalytic activity under visible light. *J. Mater. Chem. A* **2013**, *1*, 2929–3188. [CrossRef]
110. He, M.; Li, D.; Jiang, D.; Chen, M. Magnetically separable γ-Fe_2O_3@SiO_2@Ce-doped TiO_2 core-shell nanocomposites: Fabrication and visible-light-driven photocatalytic activity. *J. Solid State Chem.* **2012**, *192*, 139–143. [CrossRef]
111. Kaur, N.; Shahi, S.K.; Singh, V. Synthesis, characterization and photocatalytic activity of magnetically separable γ-Fe_2O_3/N,Fe codoped TiO_2 heterojunction for degradation of Reactive Blue 4 dye. *RSC Adv.* **2015**, *5*, 61623–61630. [CrossRef]
112. Yu, L.; Yang, X.; Wang, D. TiO_2 incorporated in magnetic mesoporous SBA-15 by a facile inner-pore hydrolysis process toward enhanced adsorption-photocatalysis performances for As(III). *J. Colloid Interface Sci.* **2015**, *448*, 525–532. [CrossRef] [PubMed]
113. Liu, Y.; Yu, L.; Hu, Y.; Guo, C.; Wen, X.; Lou, D. A magnetically separable photocatalyst based on nest-like γ-Fe_2O_3/ZnO double-shelled hollow structures with enhanced photocatalytic activity. *Nanoscale* **2012**, *4*, 183–187. [CrossRef] [PubMed]
114. Szeto, W.; Li, J.; Huang, H.; Xuan, J.; Leung, D.Y.C. Novel urchin-like Fe_2O_3@SiO_2@TiO_2 microparticles with magnetically separable and photocatalytic properties. *RSC Adv.* **2015**, *5*, 55363–55371. [CrossRef]
115. Kumar, A.; Guo, C.; Sharma, G.; Pathania, D.; Naushad, M.; Kalia, S.; Dhiman, P. Magnetically recoverable ZrO_2/Fe_3O_4/chitosan nanomaterials for enhanced sunlight driven photoreduction of carcinogenic Cr(VI) and dechlorination and mineralization of 4-chlorophenol from simulated waste water. *RSC Adv.* **2016**, *6*, 13251–13263. [CrossRef]
116. Zhao, Y.; Tao, C.; Xiao, G.; Wei, G.; Li, L.; Liu, C.; Su, H. Controlled synthesis and photocatalysis of sea urchin-like Fe_3O_4@TiO_2@Ag nanocomposites. *Nanoscale* **2016**, *8*, 5313–5326. [CrossRef]
117. Li, G.; Wong, K.H.; Zhang, X.; Hu, C.; Yu, J.C.; Chan, R.C.Y.; Wong, P.K. Degradation of Acid Orange 7 using magnetic AgBr under visible light: The roles of oxidizing species. *Chemosphere* **2009**, *76*, 1185–1191. [CrossRef] [PubMed]
118. Álvarez, P.M.; Jaramillo, J.; López-pi, F.; Plucinski, P.K. Preparation and characterization of magnetic TiO_2 nanoparticles and their utilization for the degradation of emerging pollutants in water. *Appl. Catal. B Environ.* **2010**, *100*, 338–345. [CrossRef]
119. Zhang, L.; Wang, W.; Sun, S.; Sun, Y.; Gao, E.; Zhang, Z. Elimination of BPA endocrine disruptor by magnetic BiOBr@SiO_2@Fe_3O_4 photocatalyst. *Appl. Catal. B Environ.* **2014**, *148–149*, 164–169. [CrossRef]
120. Chen, F.; Yan, F.; Chen, Q.; Wang, Y.; Han, L.; Chen, Z.; Fang, S. Fabrication of Fe_3O_4@SiO_2@TiO_2 nanoparticles supported by graphene oxide sheets for the repeated adsorption and photocatalytic degradation of rhodamine B under UV irradiation. *Dalton Trans.* **2014**, *43*, 13537–13544. [CrossRef] [PubMed]

121. Wang, H.; Wang, W. Synthesis of Fe_3O_4/N-TiO_2/Ag hollow nanospheres and their application as recyclable photocatalysts. *J. Cluster Sci.* **2016**, *27*, 403–415. [CrossRef]
122. Ma, J.; Guo, S.; Guo, X.; Ge, H. A mild synthetic route to Fe_3O_4@TiO_2-Au composites: Preparation, characterization and photocatalytic activity. *Appl. Surf. Sci.* **2015**, *353*, 1117–1125. [CrossRef]
123. Li, S.; Liang, W.; Zheng, F.; Zhou, H.; Lin, X. Lysine surface modified Fe_3O_4@SiO_2@TiO_2 microspheres-based preconcentration and photocatalysis for *in situ* selective determination of nanomolar dissolved organic and inorganic phosphorus in seawater. *Sens Actuators B Chem.* **2016**, *224*, 48–54. [CrossRef]
124. Hongfei, L.I.U.; Shengfu, J.I.; Yuanyuan, Z.; Ming, L.I. Porous TiO_2-coated magnetic core-shell nanocomposites: Preparation and enhanced photocatalytic activity. *Chin. J. Chem. Eng.* **2013**, *21*, 569–576.
125. Ma, J.; Guo, S.; Guo, X.; Ge, H.-G. Liquid-phase deposition of TiO_2 nanoparticles on core-shell Fe_3O_4@SiO_2 spheres: Preparation, characterization, and photocatalytic activity. *J. Nanopart. Res.* **2015**, *17*, 1–11. [CrossRef]
126. Rashid, J.; Barakat, M.A.; Ruzmanova, Y.; Chianese, A. Fe_3O_4/SiO_2/TiO_2 nanoparticles for photocatalytic degradation of 2-chlorophenol in simulated wastewater. *Environ. Sci. Pollut. Res.* **2015**, *22*, 3149–3157. [CrossRef] [PubMed]
127. Hamzezadeh-Nakhjavani, S.; Tavakoli, O.; Akhlaghi, S.P. Efficient photocatalytic degradation of organic pollutants by magnetically recoverable nitrogen-doped TiO_2 nanocomposite photocatalysts under visible light irradiation. *Environ. Sci. Pollut. Res.* **2015**, *22*, 18859–18873. [CrossRef] [PubMed]
128. Cao, M.; Wang, P.; Ao, Y.; Wang, C.; Hou, J.; Qian, J. Photocatalytic degradation of tetrabromobisphenol A by a magnetically separable graphene-TiO_2 composite photocatalyst: Mechanism and intermediates analysis. *Chem. Eng. J.* **2015**, *264*, 113–124. [CrossRef]
129. Li, C.; Tan, J.; Fan, X.; Zhang, B.; Zhang, H.; Zhang, Q. Magnetically separable one dimensional Fe_3O_4/P(MAA-DVB)/TiO_2 nanochains: Preparation, characterization and photocatalytic activity. *Ceram. Int.* **2015**, *41*, 3860–3868. [CrossRef]
130. Xiang, Y.; Wang, H.; He, Y.; Song, G. Efficient degradation of methylene blue by magnetically separable Fe_3O_4/chitosan/TiO_2 nanocomposites. *Desalin. Water Treat.* **2015**, *55*, 1018–1025. [CrossRef]
131. Su, W.; Zhang, T.; Li, L.; Xing, J.; He, M.; Zhong, Y.; Li, Z. Synthesis of small yolk-shell Fe_3O_4@TiO_2 nanoparticles with controllable thickness as recyclable photocatalysts. *RSC Adv.* **2014**, *4*, 8901–8906. [CrossRef]
132. Dong, X.; Shao, Y.; Zhang, X.; Ma, H.; Zhang, X.; Shi, F.; Ma, C.; Xue, M. Synthesis and properties of magnetically separable Fe_3O_4/TiO_2/Bi_2O_3 photocatalysts. *Res. Chem. Intermed.* **2014**, *40*, 2953–2961. [CrossRef]
133. Li, C.; Younesi, R.; Cai, Y.; Zhu, Y.; Ma, M.; Zhu, J. Photocatalytic and antibacterial properties of Au-decorated Fe_3O_4@mTiO_2 core-shell microspheres. *Appl. Catal. B Environ.* **2014**, *156–157*, 314–322. [CrossRef]
134. Su, J.; Zhang, Y.; Xu, S.; Wang, S.; Ding, H.; Pan, S. Highly efficient and recyclable triple-shelled Ag@Fe_3O_4@SiO_2@TiO_2 photocatalysts for degradation of organic pollutants and reduction of hexavalent chromium ions. *Nanoscale* **2014**, *6*, 5181–5192. [CrossRef] [PubMed]
135. Chen, L.; Li, L.; Wang, T.; Zhang, L.; Xing, S. A novel strategy to fabricate multifunctional Fe_3O_4@C@TiO_2 yolk-shell structures as magnetically recyclable photocatalysts. *Nanoscale* **2014**, *6*, 6603–6608. [CrossRef] [PubMed]
136. Chi, Y.; Yuan, Q.; Li, Y.; Zhao, L.; Li, N.; Li, X.; Yan, W. Magnetically separable Fe_3O_4@SiO_2@TiO_2-Ag microspheres with well-designed nanostructure and enhanced photocatalytic activity. *J. Hazard. Mater.* **2013**, *262*, 404–411. [CrossRef] [PubMed]
137. Tang, Y.; Zhang, G.; Liu, C.; Luo, S.; Xu, X.; Chen, L.; Wang, B. Magnetic TiO_2-graphene composite as a high-performance and recyclable platform for efficient photocatalytic removal of herbicides from water. *J. Hazard. Mater.* **2013**, *252–253*, 115–122. [CrossRef] [PubMed]
138. Shojaei, F.A.; Shams-Nateri, A.; Ghomashpasand, M. Comparative study of photocatalytic activities of magnetically separable WO_3/TiO_2/Fe_3O_4 nanocomposites and TiO_2, WO_3/TiO_2 and TiO_2/Fe_3O_4 under visible light irradiation. *Superlattice Microstruct.* **2015**, *88*, 211–224. [CrossRef]
139. Chidambaram, S.; Pari, B.; Kasi, N.; Muthusamy, S. ZnO/Ag heterostructures embedded in Fe_3O_4 nanoparticles for magnetically recoverable photocatalysis. *J. Alloy Compd.* **2016**, *665*, 404–410. [CrossRef]
140. Yang, J.; Wang, J.; Li, X.; Wang, D.; Song, H. Synthesis of urchin-like Fe_3O_4@SiO_2@ZnO/CdS core-shell microspheres for the repeated photocatalytic degradation of rhodamine B under visible light. *Catal. Sci. Technol.* **2016**. [CrossRef]

141. Shekofteh-Gohari, M.; Habibi-Yangjeh, A. Ultrasonic-assisted preparation of novel ternary ZnO/AgI/Fe_3O_4 nanocomposites as magnetically separable visible-light-driven photocatalysts with excellent activity. *J. Colloid Interface Sci.* **2016**, *461*, 144–153. [CrossRef] [PubMed]
142. Shekofteh-Gohari, M.; Habibi-Yangjeh, A. Novel magnetically separable ZnO/AgBr/Fe_3O_4/Ag_3VO_4 nanocomposites with tandem n–n heterojunctions as highly efficient visible-light-driven photocatalysts. *RSC Adv.* **2015**, *6*, 2402–2413.
143. Shekofteh-Gohari, M.; Habibi-Yangjeh, A. Ternary ZnO/Ag_3VO_4/Fe_3O_4 nanocomposites: Novel magnetically separable photocatalyst for efficiently degradation of dye pollutants under visible-light irradiation. *Solid State Sci.* **2015**, *48*, 177–185. [CrossRef]
144. Shekofteh-Gohari, M.; Habibi-Yangjeh, A. Novel magnetically separable Fe_3O_4@ZnO/AgCl nanocomposites with highly enhanced photocatalytic activities under visible-light irradiation. *Sep. Purif. Technol.* **2015**, *147*, 194–202. [CrossRef]
145. Shekofteh-Gohari, M.; Habibi-Yangjeh, A. Facile preparation of Fe_3O_4@AgBr-ZnO nanocomposites as novel magnetically separable visible-light-driven photocatalysts. *Ceram. Int.* **2015**, *41*, 1467–1476. [CrossRef]
146. Jia, X.; Dai, R.; Sun, Y.; Song, H.; Wu, X. One-step hydrothermal synthesis of Fe_3O_4/g-C_3N_4 nanocomposites with improved photocatalytic activities. *J. Mater. Sci.* **2016**, *27*, 3791–3798. [CrossRef]
147. Mousavi, M.; Habibi-Yangjeh, A. Magnetically separable ternary g-C_3N_4/Fe_3O_4/BiOI nanocomposites: Novel visible-light-driven photocatalysts based on graphitic carbon nitride. *J. Colloid Interface Sci.* **2016**, *465*, 83–92. [CrossRef] [PubMed]
148. Akhundi, A.; Habibi-Yangjeh, A. Novel magnetic g-C_3N_4/Fe_3O_4/AgCl nanocomposites: Facile and large-scale preparation and highly efficient photocatalytic activities under visible-light irradiation. *Mater. Sci. Semicond. Process.* **2015**, *39*, 162–171. [CrossRef]
149. Akhundi, A.; Habibi-Yangjeh, A. Novel magnetically separable g-C_3N_4/AgBr/Fe_3O_4 nanocomposites as visible-light-driven photocatalysts with highly enhanced activities. *Ceram. Int.* **2015**, *41*, 5634–5643. [CrossRef]
150. Feng, X.; Lou, X. The effect of surfactants-bound magnetite (Fe_3O_4) on the photocatalytic properties of the heterogeneous magnetic zinc oxides nanoparticles. *Sep. Purif. Technol.* **2015**, *147*, 266–275. [CrossRef]
151. Li, W.; Tian, Y.; Li, P.; Zhang, B.; Zhang, H.; Geng, W.; Zhang, Q. Synthesis of rattle-type magnetic mesoporous and investigation of its photoactivity in the degradation of methylene blue. *RSC Adv.* **2015**, *5*, 48050–48059. [CrossRef]
152. Li, X.; Wang, G.; Cheng, Y. Preparation and characteristics of Fe_3O_4-$BaTiO_3$ heterostructural nanocomposite as photocatalyst. *Res. Chem. Intermed.* **2015**, *41*, 3031–3039. [CrossRef]
153. Singh, K.K.; Senapati, K.K.; Borgohain, C.; Sarma, K.C. Newly developed Fe_3O_4-Cr_2O_3 magnetic nanocomposite for photocatalytic decomposition of 4-chlorophenol in water. *J. Environ. Sci.* **2015**. [CrossRef]
154. Cao, C.; Xiao, L.; Chen, C.; Cao, Q. Magnetically separable Cu_2O/chitosan–Fe_3O_4 nanocomposites: Preparation, characterization and visible-light photocatalytic performance. *Appl. Surf. Sci.* **2015**, *333*, 110–118. [CrossRef]
155. Cao, Y.; Li, C.; Li, J.; Li, Q.; Yang, J. Magnetically separable Fe_3O_4/AgBr hybrid materials: Highly efficient photocatalytic activity and good stability. *Nanoscale Res. Lett.* **2015**, *10*, 952. [CrossRef] [PubMed]
156. Zhong, S.; Jiang, W.; Han, M.; Liu, G.; Zhang, N.; Lu, Y. Graphene supported silver@silver chloride and ferroferric oxide hybrid, a magnetically separable photocatalyst with high performance under visible light irradiation. *Appl. Surf. Sci.* **2015**, *347*, 242–249. [CrossRef]
157. Jing, J.; Zhang, Y.; Feng, J.; Li, W.; Yu, W.W. Facile preparation and high performance of magnetically separable metalloporphyrin. *Chem. Eng. J.* **2015**, *263*, 385–391. [CrossRef]
158. Wang, B.; Zhang, M.; Li, W.; Wang, L.; Zheng, J.; Gan, W. Fabrication of Au(Ag)/AgCl/Fe_3O_4@PDA@Au nanocomposites with enhanced visible-light-driven photocatalytic activity. *Dalton Trans.* **2015**, *44*, 17020–17025. [CrossRef] [PubMed]
159. Yang, S.; Ye, C.; Song, X.; He, L.; Liao, F. Theoretical calculation based synthesis of a poly(p-phenylenediamine)–Fe_3O_4 composite: A magnetically recyclable photocatalyst with high selectivity for acid dyes. *RSC Adv.* **2014**, *4*, 54810–54818. [CrossRef]
160. An, L.; Wang, G.; Shi, X.; Su, M.; Gao, F.; Cheng, Y. Recyclable Fe_3O_4/ZnO/PPy composite photocatalyst: Fabrication and photocatalytic activity. *Russ. J. Phys. Chem. A* **2014**, *88*, 2419–2423. [CrossRef]

161. Wang, C.; Cao, M.; Wang, P.; Ao, Y.; Hou, J.; Qian, J. Preparation of a magnetic graphene oxide-Ag_3PO_4 composite photocatalyst with enhanced photocatalytic activity under visible light irradiation. *J. Taiwan Inst. Chem. Eng.* **2014**, *45*, 1080–1086. [CrossRef]
162. Peik-See, T.; Pandikumar, A.; Ngee, H.; Ming, N. Magnetically separable reduced graphene oxide/iron oxide nanocomposite materials for environmental remediation. *Catal. Sci. Technol.* **2014**, *4*, 4396–4405. [CrossRef]
163. Li, Z.; Wen, Y.; Shang, J.; Wu, M.; Wang, L.; Guo, Y. Magnetically recoverable Cu_2O/Fe_3O_4 composite photocatalysts: Fabrication and photocatalytic activity. *Chin. Chem. Lett.* **2014**, *25*, 287–291. [CrossRef]
164. Cao, X.; Chen, Y.; Jiao, S.; Fang, Z.; Xu, M.; Liu, X.; Li, L.; Pang, G.; Feng, S. Magnetic photocatalysts with a p–n junction: Fe_3O_4 nanoparticle and $FeWO_4$ nanowire heterostructures. *Nanoscale* **2014**, *6*, 12366–12370. [CrossRef] [PubMed]
165. Wang, H.; Wei, Z.; Matsui, H.; Zhou, S. Fe_3O_4/carbon quantum dots hybrid nanoflower for highly active and recyclable visible-light driven. *J. Mater. Chem. A* **2014**, *2*, 15740–15745. [CrossRef]
166. Zhang, D.; Pu, X.; Gao, Y.; Su, C.; Li, H.; Li, H. One-step combustion synthesis of $CoFe_2O_4$-graphene hybrid materials for photodegradation of methylene blue. *Mater. Lett.* **2013**, *113*, 179–181. [CrossRef]
167. Zhu, H.; Jiang, R.; Huang, S.; Yao, J.; Fu, F.; Li, J. Novel magnetic $NiFe_2O_4$/multi-walled carbon nanotubes hybrids: Facile synthesis, characterization, and application to the treatment of dyeing wastewater. *Ceram. Int.* **2015**, *41*, 11625–11631. [CrossRef]
168. Bai, S.; Shen, X. One-pot solvothermal preparation of magnetic reduced graphene oxide-ferrite hybrids for organic dye removal. *Carbon* **2012**, *50*, 2337–2346. [CrossRef]
169. Sun, J.; Fu, Y.; Xiong, P.; Sun, X.; Xu, B.; Wang, X. A magnetically separable P25/$CoFe_2O_4$/graphene catalyst with enhanced adsorption capacity and visible-light-driven photocatalytic activity. *RSC Adv.* **2013**, *3*, 22490–22497. [CrossRef]
170. Xiong, P.; Zhu, J.; Wang, X. Cadmium sulfide-ferrite nanocomposite as a magnetically recyclable photocatalyst with enhanced visible-light-driven photocatalytic activity and photostability. *Ind. Eng. Chem. Res.* **2013**, *52*, 17126–17133. [CrossRef]
171. Fu, Y.; Chen, Q.; He, M.; Wan, Y.; Sun, X.; Xia, H.; Wang, X. Copper ferrite-graphene hybrid: A multifunctional heteroarchitecture for photocatalysis and energy storage. *Ind. Eng. Chem. Res.* **2012**, *51*, 11700–11709. [CrossRef]
172. Ji, H.; Jing, X.; Xu, Y.; Yan, J.; Li, H.; Li, Y.; Huang, L.; Zhang, Q.; Xu, H.; Li, H. Magnetic g-$C_3N_4/NiFe_2O_4$ hybrids with enhanced photocatalytic activity. *RSC Adv.* **2015**, *5*, 57960–57967. [CrossRef]
173. Zhang, W.; Wang, M.; Zhao, W.; Wang, B. Magnetic composite photocatalyst $ZnFe_2O_4/BiVO_4$: Synthesis, characterization, and visible-light photocatalytic activity. *Dalton Trans.* **2013**, *42*, 15464–15474. [CrossRef] [PubMed]
174. Yao, Y.; Cai, Y.; Lu, F.; Qin, J.; Wei, F.; Xu, C.; Wang, S. Magnetic $ZnFe_2O_4$-C_3N_4 hybrid for photocatalytic degradation of aqueous organic pollutants by visible light. *Ind. Eng. Chem. Res.* **2014**, *53*, 17294–17302. [CrossRef]
175. Wu, S.; Wang, P.; Cai, Y.; Liang, D.; Ye, Y.; Tian, Z.; Liu, J.; Linag, C. Reduced graphene oxide anchored magnetic $ZnFe_2O_4$ nanoparticles with enhanced visible-light photocatalytic activity. *RSC Adv.* **2015**, *5*, 9069–9074. [CrossRef]
176. Yang, D.; Feng, J.; Jiang, L.; Wu, X.; Sheng, L.; Jiang, Y.; Wei, T.; Fan, Z. Photocatalyst interface engineering: Spatially confined growth of $ZnFe_2O_4$ within graphene networks as excellent visible-light-driven photocatalysts. *Adv. Funct. Mater.* **2015**, *25*, 7080–7087. [CrossRef]
177. Khadgi, N.; Li, Y.; Upreti, A.R.; Zhang, C.; Zhang, W.; Wang, Y.; Wang, D. Enhanced photocatalytic degradation of 17 α-ethinylestradiol exhibited by multifunctional $ZnFe_2O_4$-Ag/rGO nanocomposite under visible light. *Photochem. Photobiol.* **2016**, *92*, 238–246. [CrossRef] [PubMed]
178. Chen, X.; Dai, Y.; Guo, J.; Liu, T.; Wang, X. Novel magnetically separable reduced graphene oxide (RGO)/$ZnFe_2O_4/Ag_3PO_4$ nanocomposites for enhanced photocatalytic performance toward 2,4-dichlorophenol under visible light. *Ind. Eng. Chem. Res.* **2016**, *55*, 568–578. [CrossRef]
179. Kulkarni, S.D.; Kumbar, S.; Menon, S.G.; Choudhari, K.S.; Santhosh, C. Magnetically separable core-shell $ZnFe_2O_4$@ZnO nanoparticles for visible light photodegradation of methyl orange. *Mater. Res. Bull.* **2016**, *77*, 70–77. [CrossRef]

180. Yao, Y.; Qin, J.; Chen, H.; Wei, F.; Liu, X.; Wang, J.; Wang, S. One-pot approach for synthesis of N-doped $TiO_2/ZnFe_2O_4$ hybrid as an efficient photocatalyst for degradation of aqueous organic pollutants. *J. Hazard. Mater.* **2015**, *291*, 28–37. [CrossRef] [PubMed]
181. Wu, S.; Shen, X.; Zhu, G.; Zhou, H.; Ji, Z.; Chen, K. Synthesis of ternary $Ag/ZnO/ZnFe_2O_4$ porous and hollow nanostructures with enhanced photocatalytic activity. *Appl. Catal. B Environ.* **2016**, *184*, 328–336. [CrossRef]
182. Ren, A.; Liu, C.; Hong, Y.; Shi, W.; Lin, S.; Li, P. Enhanced visible-light-driven photocatalytic activity for antibiotic degradation using magnetic $NiFe_2O_4/Bi_2O_3$ heterostructures. *Chem. Eng. J.* **2014**, *258*, 301–308. [CrossRef]
183. Fu, Y.; Chen, H.; Sun, X.; Wang, X. Graphene-supported nickel ferrite: A magnetically separable photocatalyst with high activity under visible light. *Am. Inst. Chem. Eng. J.* **2012**, *58*, 3298–3305. [CrossRef]
184. Patil, S.S.; Tamboli, M.S.; Deonikar, V.G.; Umarji, G.G.; Ambekar, J.D.; Kulkarni, M.V.; Kolekar, S.S.; Kale, B.B.; Patil, D.R. Magnetically separable $Ag_3PO_4/NiFe_2O_4$ composites with enhanced photocatalytic activity. *Dalton Trans.* **2015**, *44*, 20426–20434. [CrossRef] [PubMed]
185. Kim, S.H.; Kim, D.; Kwak, S.B.; Han, B.G.; Um, M.; Kang, M. Synthesis of magnetically separable core@shell structured $NiFe_2O_4@TiO_2$ nanomaterial and its use for photocatalytic hydrogen production by methanol/water splitting. *Chem. Eng. J.* **2014**, *243*, 272–279. [CrossRef]
186. Ge, M.; Hu, Z. Novel magnetic $AgBr/NiFe_2O_4$ composite with enhanced visible light photocatalytic performance. *Ceram. Int.* **2016**, *42*, 6510–6514. [CrossRef]
187. Xiong, P.; Fu, Y.; Wang, L.; Wang, X. Multi-walled carbon nanotubes supported nickel ferrite: A magnetically recyclable photocatalyst with high photocatalytic activity on degradation of phenols. *Chem. Eng. J.* **2012**, *195–196*, 149–157. [CrossRef]
188. Li, C.; Wang, J.; Wang, B.; Ru, J.; Lin, Z. A novel magnetically separable $TiO_2/CoFe_2O_4$ nanofiber with high photocatalytic activity under UV-vis light. *Mater. Res. Bull.* **2012**, *47*, 333–337. [CrossRef]
189. Wilson, A.; Mishra, S.R.; Gupta, R.; Ghosh, K. Preparation and photocatalytic properties of hybrid core-shell reusable $CoFe_2O_4$-ZnO nanospheres. *J. Magn. Magn. Mater.* **2012**, *324*, 2597–2601. [CrossRef]
190. Pongwan, P.; Inceesungvorn, B.; Phanichphant, S.; Wetchakun, N. Synthesis and characterization of a magnetically separable $CoFe_2O_4/TiO_2$ nanocomposite for the photomineralization of formic acid. *Ferroelectrics* **2013**, *453*, 133–140. [CrossRef]
191. Wetchakun, N.; Chaiwichain, S.; Wetchakun, K. Synthesis and characterization of novel magnetically separable $CoFe_2O_4/CeO_2$ nanocomposite photocatalysts. *Mater. Lett.* **2013**, *113*, 76–79. [CrossRef]
192. Gan, L.; Shang, S.; Wah, C.; Yuen, M.; Jiang, S.; Hu, E. Hydrothermal synthesis of magnetic $CoFe_2O_4$/graphene nanocomposites with improved photocatalytic activity. *Appl. Surf. Sci.* **2015**, *351*, 140–147. [CrossRef]
193. Singh, S.; Khare, N. Magnetically separable, $CoFe_2O_4$ decorated CdS nanorods for enhanced visible light driven photocatalytic activity. *Mater. Lett.* **2015**, *161*, 64–67. [CrossRef]
194. Haw, C.; Chiu, W.; Rahman, S.A.; Khiew, P.; Radiman, S.; Shukor, R.A.; Hamid, M.A.A.; Ghazali, N. The design of new magnetic-photocatalyst nanocomposites ($CoFe_2O_4$-TiO_2) as smart nanomaterials for recyclable-photocatalysis applications. *New J. Chem.* **2016**, *40*, 1124–1136. [CrossRef]
195. Choi, Y.I.; Kim, Y.; Cho, D.W.; Kang, J.; Leung, K.T.; Sohn, Y. Recyclable magnetic $CoFe_2O_4/BiOX$ (X = Cl, Br and I) microflowers for photocatalytic treatment of water contaminated with methyl orange, rhodamine B, methylene blue, and a mixed dye. *RSC Adv.* **2015**, *5*, 79624–79634. [CrossRef]
196. Xu, Y.; Zhou, T.; Huang, S.; Xie, M.; Li, H.; Xu, H. Preparation of magnetic $Ag/AgCl/CoFe_2O_4$ composites with high photocatalytic and antibacterial ability. *RSC Adv.* **2015**, *5*, 41475–41483. [CrossRef]
197. Shi, B.; Wan, J.; Liu, C.; Yu, X. Synthesis of $CoFe_2O_4$/MCM-41/TiO_2 composite microspheres and its performance in degradation of phenol. *Mater. Sci. Semicond. Process.* **2015**, *37*, 241–249. [CrossRef]
198. Gaikwad, P.N.; Hankare, P.P.; Wandre, T.M.; Garadkar, K.M.; Sasikala, R. Photocatalytic performance of magnetically separable Fe,N co-doped TiO_2-cobalt ferrite nanocomposite. *Mater. Sci. Eng. B* **2016**, *205*, 40–45. [CrossRef]
199. Manikandan, A.; Durka, M.; Seevakan, K.; Antony, S.A. A novel one-pot combustion synthesis and opto-magnetic properties of magnetically separable spinel $Mn_xMg_{1-x}Fe_2O_4$ ($0.0 \leqslant x \leqslant 0.5$) nanophotocatalysts. *J. Supercond. Novel Magn.* **2015**, *28*, 1405–1416. [CrossRef]

200. Tio, A.; Nife, O.; Nicola, D.; Vanags, M. Ag sensitized TiO_2 and $NiFe_2O_4$ three-component nanoheterostructures: Synthesis, electronic structure and strongly enhanced visible light. *RSC Adv.* **2016**, *6*, 18834–18842.
201. Chen, C.-C.; Fu, Y.-P.; Hu, S.-H. Characterizations of TiO_2/SiO_2/Ni-Cu-Zn ferrite composite for magnetic photocatalysts. *J. Am. Chem. Soc.* **2015**, *98*, 2803–2811. [CrossRef]
202. Sathishkumar, P.; Viswanathan, R. $CoFe_2O_4/TiO_2$ nanocatalysts for the photocatalytic degradation of Reactive Red 120 in aqueous solutions in the presence and absence of electron acceptors. *Chem. Eng. J.* **2013**, *220*, 302–310. [CrossRef]
203. Kadi, M.W.; Mohamed, R.M. Environmental remediation of aqueous cyanide by photocatalytic oxidation using a $NiFe_2O_4/TiO_2$-SiO_2 core-shell nanocomposite. *Desalin. Water Treat.* **2016**, *56*, 1940–1948. [CrossRef]
204. Su, R.N.; Lv, P.; Li, M.; Zhang, X.; Li, M.; Niu, J. Fabrication of $MgFe_2O_4$-ZnO heterojunction photocatalysts for application of organic pollutants. *Mater. Lett.* **2014**, *122*, 201–204. [CrossRef]
205. Leng, C.; Wei, J.; Liu, Z. Facile synthesis of PANI-modified $CoFe_2O_4$-TiO_2 hierarchical flower-like nanoarchitectures with high photocatalytic activity. *J. Nanopart. Res.* **2013**, *15*, 1643. [CrossRef]
206. Sun, A.; Chen, H.; Song, C.; Jiang, F.; Wang, X.; Fu, Y. Magnetic $Bi_{25}FeO_{40}$-graphene catalyst and its high visible-light photocatalytic performance. *RSC Adv.* **2013**, *3*, 4332–4340. [CrossRef]
207. Xie, T.; Xu, L.; Liu, C.; Yang, J.; Wang, M. Magnetic composite BiOCl-$SrFe_{12}O_{19}$:A novel p–n type heterojunction with enhanced photocatalytic activity. *Dalton Trans.* **2014**, *43*, 2211–2220. [CrossRef] [PubMed]
208. Bhukal, S.; Bansal, S.; Singhal, S. Magnetic Mn substituted cobalt zinc ferrite systems: Structural, electrical and magnetic properties and their role in photo-catalytic degradation of methyl orange azo dye. *Physica B* **2014**, *445*, 48–55. [CrossRef]
209. Qasim, M.; Asghar, K.; Raj, B.; Prathapani, S.; Khan, W.; Naqvi, A.H.; Das, D. Magnetically recyclable $Ni_{0.5}Zn_{0.5}Fe_2O_4/Zn_{0.95}Ni_{0.05}O$ nano-photocatalyst: Structural, optical, magnetic and photocatalytic properties. *Spectrochim. Acta A* **2015**, *137*, 1348–1356. [CrossRef] [PubMed]
210. Manikandan, A.; Antony, S.A. Magnetically separable $Mn_xZn_{1-x}Fe_2O_4$; ($0.0 \leqslant x \leqslant 0.5$) nanostructures: Structural, morphological, opto-magnetic and photocatalytic properties. *Synth. React. Inorg. Met-Org. Nano-Met. Chem.* **2016**. [CrossRef]
211. Shakir, I.; Sarfraz, M.; Ali, Z.; Aboud, M.F.A. Magnetically separable and recyclable graphene-$MgFe_2O_4$ nanocomposites for enhanced photocatalytic applications. *J. Alloy. Compd.* **2016**, *660*, 450–455. [CrossRef]
212. Bhukal, S.; Singhal, S. Magnetically separable copper substituted cobalt-zinc nano-ferrite photocatalyst with enhanced photocatalytic activity. *Mater. Sci. Semicond. Process.* **2014**, *26*, 467–476. [CrossRef]
213. Liu, F.; Xie, Y.; Yu, C.; Liu, X.; Dai, Y. Novel hybrid Sr-doped TiO_2/magnetic $Ni_{0.6}Zn_{0.4}Fe_2O_4$ for enhanced separation and photodegradation of organics under visible light. *RSC Adv.* **2015**, *5*, 24056–24063. [CrossRef]
214. Vignesh, K.; Suganthi, A.; Min, B.-K.; Kang, M. Photocatalytic activity of magnetically recoverable $MnFe_2O_4$/g-C_3N_4/TiO_2 nanocomposite under simulated solar light irradiation. *J. Mol. Catal. A Chem.* **2014**, *395*, 373–383. [CrossRef]
215. He, H.-Y. Photocatalytic degradations of dyes on magnetically separable $Ni_{1-x}Co_xFe_2O_4$ nanoparticles synthesized by a hydrothermal process. *Part. Sci. Technol.* **2016**, *34*, 143–151. [CrossRef]
216. Zhang, Z.; Xu, L.; Liu, C. Preparation and characterization of composite magnetic photocatalyst $Mn_xZn_{1-x}Fe_2O_4/\beta$-$Bi_2O_3$. *RSC Adv.* **2015**, *5*, 79997–80004. [CrossRef]
217. He, H.; Yan, Y.; Huang, J.; Lu, J. Rapid photodegradation of methyl blue on magnetic $Zn_{1-x}Co_xFe_2O_4$ nanoparticles synthesized by hydrothermal process. *Sep. Purif. Technol.* **2014**, *136*, 36–41. [CrossRef]
218. Shi, Y.; Zhou, K.; Wang, B.; Jiang, S.; Qian, X.; Gui, Z.; Yuen, R.K.K.; Hu, Y. Ternary graphene-$CoFe_2O_4$/CdS nanohybrids: Preparation and application as recyclable photocatalysts. *J. Mater. Chem. A* **2014**, *2*, 535–544. [CrossRef]
219. Sathishkumar, P.; Pugazhenthiran, N. ZnO supported $CoFe_2O_4$ nanophotocatalysts for the mineralization of Direct Blue 71 in aqueous environments. *J. Hazard. Mater.* **2013**, *252–253*, 171–179. [CrossRef] [PubMed]